Nanowire Solar Cells

Erik C. Garnett, Mark L. Brongersma, Yi Cui,
and Michael D. McGehee

Department of Materials Science, Stanford University, Stanford, California 94305-4045;
email: egarnett@stanford.edu, brongersma@stanford.edu, yicui@stanford.edu,
mmcgehee@stanford.edu

Keywords

photovoltaics, nanoscience, light trapping, energy, solar cells

Abstract

The nanowire geometry provides potential advantages over planar wafer-based or thin-film solar cells in every step of the photoconversion process. These advantages include reduced reflection, extreme light trapping, improved band gap tuning, facile strain relaxation, and increased defect tolerance. These benefits are not expected to increase the maximum efficiency above standard limits; instead, they reduce the quantity and quality of material necessary to approach those limits, allowing for substantial cost reductions. Additionally, nanowires provide opportunities to fabricate complex single-crystalline semiconductor devices directly on low-cost substrates and electrodes such as aluminum foil, stainless steel, and conductive glass, addressing another major cost in current photovoltaic technology. This review describes nanowire solar cell synthesis and fabrication, important characterization techniques unique to nanowire systems, and advantages of the nanowire geometry.

1. INTRODUCTION

Over the past decade, both solar cell research and nanowire research have become hot topics within science and engineering (1–6). The need for higher solar cell efficiencies at lower cost has become apparent, and at the same time synthetic control in nanoscience has improved such that high-performance electronic devices are becoming possible (7–10). Nanowire solar cells have some potential benefits over traditional wafer-based or thin-film devices related to optical, electrical, and strain relaxation effects; new charge separation mechanisms; and cost. Ordered arrays of vertical nanowires with radial junctions take advantage of all these effects, although solar cells made using axial junctions or random arrays can still have some benefits over planar cells, as shown schematically in **Figure 1** and described in detail in Section 3. Even in the optimal configuration, it is unlikely that nanowire cells will exceed the efficiency limits of planar devices; instead, they relax the requirements needed to approach those limits, opening up the door to low-cost, previously discarded materials and processing options. Functioning nanowire photovoltaics have been fabricated using a wide variety of materials including silicon, germanium, zinc oxide, zinc sulfide, cadmium telluride, cadmium selenide, copper oxide, titanium oxide, gallium nitride, indium gallium nitride, gallium arsenide, indium arsenide, and many polymer/nanowire combinations (7, 11–24). Output efficiencies have steadily increased so that most material systems have now achieved efficiencies higher than 1%, with some close to 10%, but a number of unresolved questions must be answered before such materials can be used in commercial devices. This review discusses the synthetic approaches used to fabricate nanowire array and single-nanowire solar cells, describes important characterization techniques (especially those that differ substantially from bulk), details the benefits that nanowires can provide, and gives an outlook on challenges and opportunities for the nanowire solar cell field.
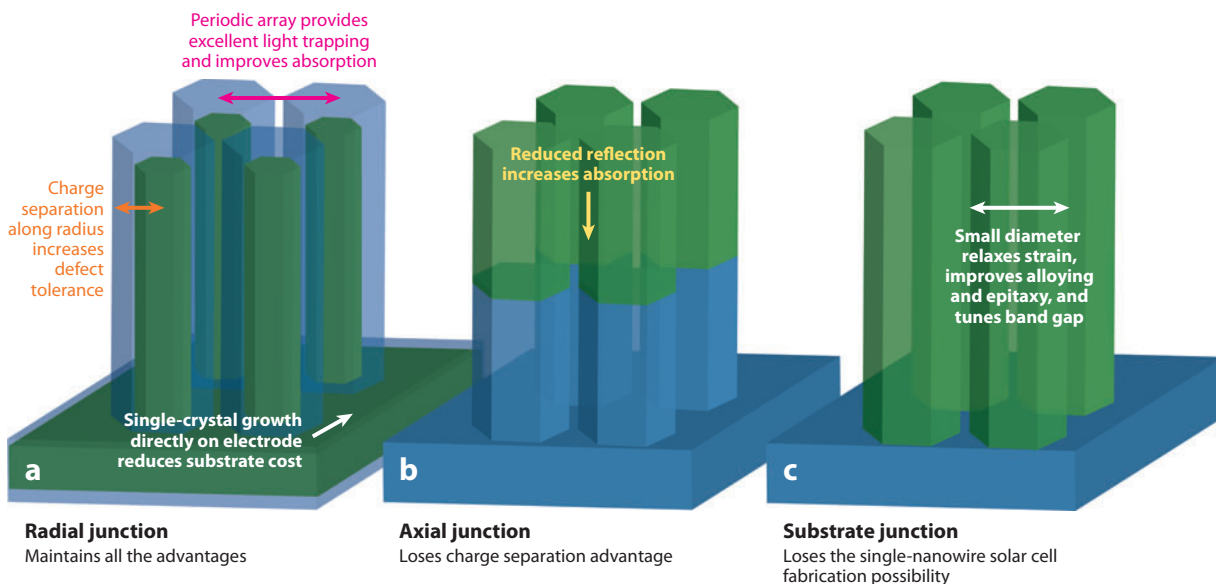

Figure 1

Benefits of the nanowire geometry. (*a*) Periodic arrays of nanowires with radial junctions maintain all the advantages, including reduced reflection, extreme light trapping, radial charge separation, relaxed interfacial strain, and single-crystalline synthesis on nonepitaxial substrates. (*b*) Axial junctions lose the radial charge separation benefit but keep the others. (*c*) Substrate junctions lack the radial charge separation benefit and cannot be removed from the substrate to be tested as single-nanowire solar cells.

2. NANOWIRE SOLAR CELL FABRICATION AND ANALYSIS

Nanowire solar cell fabrication and analysis consist of four primary steps that are described in detail below: nanowire synthesis, junction formation, contacting, and characterization.

2.1. Nanowire Synthesis

A huge body of literature is now devoted to nanowire synthesis, and excellent reviews describe the growth mechanisms (2, 3, 25, 26). Here we focus on the two techniques most commonly used in nanowire solar cells: chemical vapor deposition and patterned chemical etching.

In chemical vapor deposition, nanowires are synthesized by flowing chemical precursor vapors into the hot zone of a furnace to react on a substrate, often with the assistance of a metal catalyst nanoparticle. The vapor source can be a gas, liquid, or heated solid. The precursor vapors are transported to the substrate with an inert carrier gas, often combined with other reactant gases along the way. The substrate is placed in the deposition zone of the furnace, where chemical decomposition is favorable. A number of mechanisms promote nanowire growth instead of uniform thin-film deposition. The most commonly cited is the vapor-liquid-solid (VLS) mechanism, which uses a metal catalyst that forms a liquid eutectic with the desired nanowire material (25, 27). Upon chemical decomposition and dissolution into the liquid eutectic droplet, the solution becomes supersaturated and overcomes the nucleation barrier to begin precipitation. Additional flux of dissolved species leads to further precipitation and nanowire growth. With the proper substrate, precursor, temperature, catalyst, and concentration, vertical nanowire growth is possible (28), which is advantageous for solar cells, as is described in Section 3. Catalyst patterning approaches allow for ordered nanowire array synthesis (14).

Dopants can be introduced during growth or in a separate diffusion step (29, 30). In situ doping has the advantage of being able to occur at lower temperatures because it does not rely exclusively on diffusion but can be incorporated through the catalyst (29). Unlike in situ doping, ex situ doping does not affect the nanowire or thin-film growth kinetics and decouples the growth and doping time and temperature (30–32). Measuring the dopant concentration and distribution in nanowire systems is significantly more difficult than in bulk wafers or thin films and is discussed in Section 2.4. Although the VLS growth mechanism is common in nanowires grown by chemical vapor deposition, a number of other mechanisms are also possible; these include vapor-solid-solid (VSS), vapor-solid (VS), and dislocation-mediated growth (3, 33–36). The VSS mechanism is similar to VLS growth, but the catalyst remains solid instead of forming a eutectic liquid. This phase difference means that chemical concentration and precipitation are not the dominant driving forces for 1-D growth in the VSS mechanism; instead, the catalyst accelerates precursor decomposition. The VS mechanism does not use a catalyst and instead relies on a difference in surface energy between the crystal planes that cap the nanowire to drive 1-D growth. The dislocation-mediated growth mechanism uses high-energy defect sites to incorporate atoms along a screw dislocation, which leads to 1-D growth in the same way that a spiral staircase leads upward.

Patterned chemical etching is a top-down or hybrid top-down/bottom-up approach that involves a lithography step followed by an etch step. **Figure 2** shows the fabrication steps for one possible hybrid scheme and images of the resulting nanowire array. The initial lithography step is either a top-down approach such as e-beam and nanoimprint or a spontaneous bottom-up approach such as nanosphere assembly, anodic alumina, and block copolymer formation (14, 37–40). The patterned substrate is dissolved with a directional, substrate-selective etch such as deep reactive-ion etching (DRIE) or metal-assisted chemical etching (40–43). The nanosphere assembly patterning approach is particularly useful, as it provides a method for controlling the
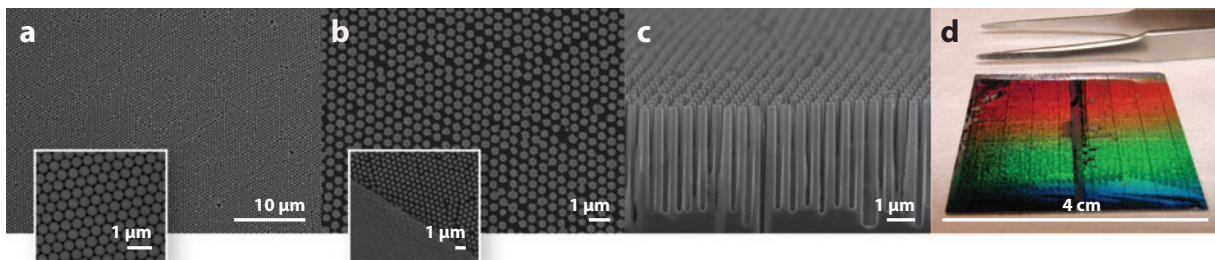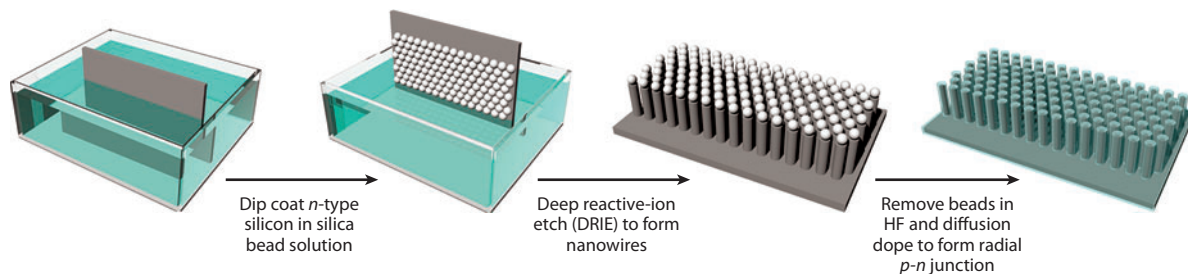
Figure 2

Nanowire solar cell fabrication. (*Top row*) Schematic of the fabrication process. HF denotes hydrofluoric acid. (*a*) Scanning electron microscopy (SEM) image of a close-packed monolayer of silica beads assembled on a silicon wafer using dip coating. (*b*) Plan-view SEM image of a completed ordered silicon nanowire radial *p-n* junction array solar cell made by bead assembly and deep reactive-ion etching. The inset shows the edge of a top contact finger, demonstrating that the metal completely fills in between the nanowires. (*c*) Tilted cross-sectional SEM of the solar cell in panel *b*. (*d*) Tilted optical image of 36 silicon nanowire radial *p-n* junction solar cell arrays from panels *a–c*. The color dispersion demonstrates the excellent periodicity present over the entire substrate. Adapted with permission from Reference 11. Copyright © 2010, American Chemical Society.

nanowire diameter and pitch independently simply by changing the sphere diameter and etch time prior to the substrate etch step (42). Silica and polymer spheres can be synthesized with a wide range of diameters (typically 100–1,000 nm) and can be assembled over large areas using Langmuir-Blodgett, dip-coating, and roll-coating methods (11, 42, 44, 45). Anodic alumina and block copolymer templates can access much smaller pattern dimensions (typically 10–100 nm) and have been used to fabricate nanowires with diameters of ∼10 nm (39, 43). The patterned chemical etching technique has the advantage that the starting wafer or thin film sets the doping level and material composition, which allows for more precise control over the material parameters and simplifies the material characterization.

2.2. Junction Formation

Once the nanowire has been synthesized, a junction must be introduced to promote charge separation and collection. This junction can occur along the diameter (radial separation) or length (axial separation) of the nanowire or at the substrate interface (**Figure 1**). The only requirement for the junction is that it induces a chemical potential difference that causes electrons and holes to move in opposite directions to allow for carrier collection. The first type of junction used in nanowire solar cells is known as a *p-n* junction or homojunction. In this case, a single semiconductor material is used, and either extrinsic dopant atoms or intrinsic defects are introduced in different regions of the nanowire to create the chemical potential difference. Dopants can be introduced by diffusion
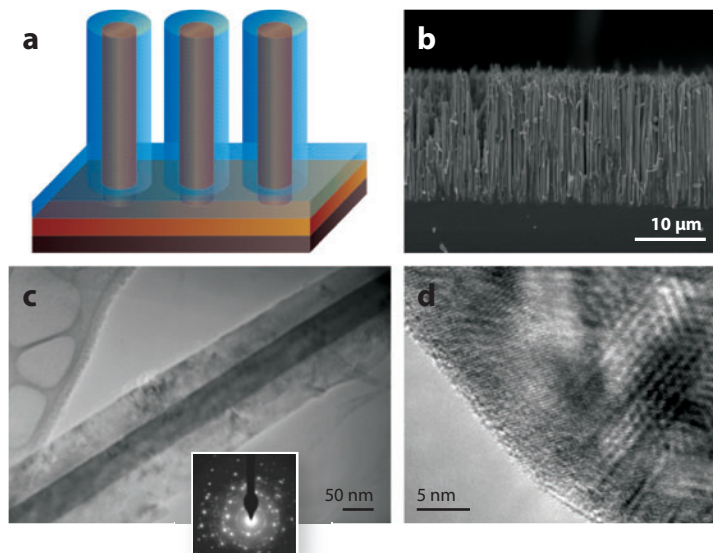
Figure 3

Silicon nanowire solar cell structure. (*a*) Schematic cell design with the single-crystalline *n*-Si nanowire core
in brown, the polycrystalline *p*-Si shell in blue, and the back contact in black. (*b*) Cross-sectional scanning
electron microscopy image of a completed device demonstrating excellent vertical alignment and dense wire
packing. (*c*) Transmission electron microscopy (TEM) image showing the single-crystalline *n*-Si core and
the polycrystalline *p*-Si shell. The inset is the selected area electron diffraction pattern. (*d*) TEM image from
the edge of the core-shell nanowire showing nanocrystalline domains. Reprinted with permission from
Reference 41. Copyright © 2008, American Chemical Society.

or by depositing a thin film over the original nanowire (11, 41, 46, 47). In the diffusion case, if
the time is too long or the temperature too high, the nanowires can be converted completely to
the opposite carrier type (to give a nanowire substrate junction, as in **Figure 1**), in which case
the benefits of the radial junction are lost (48–50). However, the lower junction area can also lead
to higher efficiencies when the starting wafer is very pure. In the thin-film deposition case, the
shell must be doped with a carrier type that is opposite to that of the nanowire and can be single
crystalline if grown epitaxially but more often is polycrystalline (**Figure 3**). Most commercially
available solar cells, including silicon (both crystalline and amorphous), gallium arsenide, and
high-efficiency multijunction cells, use a homojunction to separate carriers (51).

The second type of solar cell uses a Schottky junction to separate charges. Schottky cells use
a metal (or very highly doped semiconductor) with a large (or small) work function in contact
with an *n*-type (or a *p*-type) semiconductor to induce a depletion region or even inversion at the
semiconductor surface. This leads to a barrier for carrier flow in only one direction. From a band
diagram perspective, this case is very similar to the *p*-*n* junction. However, the semiconductor/
metal interface must have a low defect density; otherwise, there will be Fermi-level pinning, and
the solar cell will have a much lower output voltage than theoretically possible (51, 52). Conductive
polymers have been used in conjunction with silicon nanowires to form Schottky junction solar
cells (53). Semiconductor-electrolyte (photoelectrochemical) solar cells use an electrolyte as the
metal and are the most common nanowire Schottky cells (54–57).

The third type of solar cell, termed a heterojunction, uses a type II band offset (one material has
higher conduction and valence bands than the other) between two different materials to separate

carriers. The type II offset is preferred over a type I offset (in the latter, one material straddles both bands of the other material) because it helps ensure that electron and hole transfer occurs primarily in the desired direction. Many popular thin-film solar materials, including cadmium telluride, copper indium gallium selenide (CIGS), copper zinc tin sulfide/selenide (CZTS), and organics, typically use heterojunctions to separate charge carriers (58–61). Dye-sensitized solar cells are a special type of heterojunction cell that require a redox couple to regenerate the surface-adsorbed dye after photoexcitation and electron injection. Nanowire heterojunctions are usually fabricated by depositing a thin film on top of a nanowire array via standard methods such as chemical vapor deposition, pulsed laser deposition, electrodeposition, or chemical bath deposition for inorganic materials and spin coating or solution dye adsorption for organics and dye cells (13, 14, 22, 62–64). Quantum dots attached to the nanowire surface can be used instead of dyes to absorb light in dye-sensitized solar cells (65). Inorganic nanoparticles have also been used to infiltrate nanowire arrays; the subsequent annealing or ligand exchange allows for improved charge transport between nanoparticles (16, 66).

2.3. Contacts

After the nanowires are grown and the junction is formed, contacts must be deposited to extract electrons and holes. As in planar solar cells, ohmic contacts maximize the open-circuit voltage (V_{oc}), short-circuit current density (J_{sc}), fill factor (*FF*), and overall energy conversion efficiency (η). Methods for making ohmic contacts in planar solar cells, such as heavy doping and interfacial layers, also apply to nanowire systems (11, 30, 46, 51, 58). Clearly, Schottky junction solar cells require one Schottky and one ohmic contact, as discussed in Section 2.2.

Single-nanowire solar cells are usually contacted using e-beam or photolithography and metal evaporation. Radial junctions (core-shell) require multiple lithography and etch steps so that electrons and holes can be extracted separately (20, 47). Nanowire array contacting schemes are typically similar to those of planar thin-film solar cells. The bottom or top contact must be transparent to allow light to come through, and the other contact is usually made of reflective metal. Obtaining conformal (or at least continuous) metal finger grids or transparent conductor coatings on high-aspect-ratio structures can be challenging and often requires a much thicker layer and more uniform deposition techniques (such as sputtering or electrodeposition) than in planar cells (11). If the junction is made by deposition, the nanowire diameters can expand to the point at which they begin to touch or possibly even fuse together completely, simplifying the contacting scheme (14, 41). Semiconductor-electrolyte junctions provide the simplest uniform contact (54–57).

2.4. Device Geometries and Characterization

Nanowire solar cells can be made from individual nanowires or arrays. Single-nanowire devices enable careful study of fundamental processes such as charge transfer, surface recombination, and minority carrier diffusion. They also simplify analysis of dopant density, surface state, and conductivity measurements by removing ensemble averaging and nonuniform contacting effects. However, they cannot be used to compare nanowire devices with standard planar technology or to investigate phenomena that depend on an array or vertical geometry such as photonic crystal light trapping or absorption/charge separation orthogonalization effects.

Single-nanowire studies are important to understand transport, doping, surface, and charge separation properties. However, unlike in bulk wafer or thin-film materials, for single nanowires, extracting carrier concentration, mobility, dopant profiles, surface state densities, minority carrier

diffusion lengths, and metal impurity concentrations is not straightforward. Hall effect measurements, secondary ion mass spectrometry (SIMS), Auger electron spectroscopy (AES), and X-ray photoelectron spectroscopy (XPS) cannot be implemented with the resolution necessary to obtain meaningful results, so traditional transport measurements are the primary tool for extracting these properties. The most common measurement is the back-gated or top-gated field-effect transistor (FET), which is often used to determine mobility and carrier concentration in thin films. **Figure 4** shows a schematic and corresponding scanning electron microscopy (SEM) images of a single-nanowire FET that has both a top gate and a back gate. In this case, the nanowire was grown epitaxially between degenerately doped silicon source and drain electrodes, but a similar structure can be prepared by drop casting nanowires on a substrate and by using e-beam lithography to define metal source and drain electrode contacts.
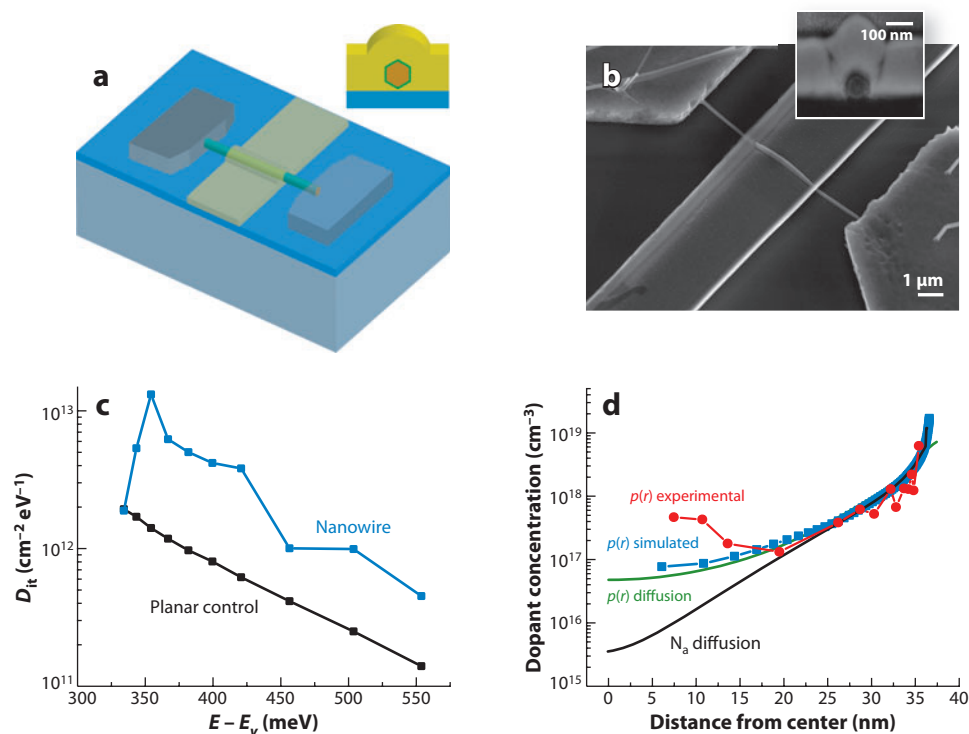

Figure 4

Device structure, interface state density, and radial dopant profile. (*a*) Schematic of the capacitance-voltage (C-V) device structure with p^+-Si source and drain pads (*gray*), SiO_2 buried oxide (*blue*), p^+-Si back gate (*gray*), *p*-Si nanowire (*orange*), atomic layer deposition Al_2O_3 surround gate oxide (*green*), and chromium surround gate metal (*yellow*). (*Inset*) Cross-sectional schematic view with a hexagonally faceted silicon nanowire. (*b*) Scanning electron microscopy image of an actual nanowire device. (*Inset*) A cross-sectional view of the device taken after focused ion beam milling. (*c*) Interface state density D_{it} versus energy in the band gap with respect to the valence band energy ($E - E_v$) extracted from the 200-Hz and 20-kHz C-V curves using the high-low method for both nanowire (*blue*) and planar control (*black*) samples. (*d*) Radial dopant distribution extracted from the experimental C-V curve (*red*) compared with the simulated boron diffusion profile (*black*), the calculated majority carrier redistribution using the simulated dopant profile as an input (*green*), and the carrier concentration extracted from the theoretical C-V curve with the simulated boron profile as an input (*blue*). N_a denotes the acceptor concentration. Adapted from Reference 30.

Due to uncertainties in the gate capacitance, surface depletion effects, and nonuniform dopant distribution, the extracted mobility and carrier concentration values can have substantial errors when standard assumptions are used. Khanal & Wu (67) used finite element method (FEM) simulations to show that mobility measurements can have an error between approximately a factor of two and ten when the infinite cylinder on a plane model is used for the capacitance. The higher error occurred in low-doped nanowires with small diameters and thin back-gate oxides (67). Top-gate capacitance measurements on germanium nanowires showed that the gate capacitance error could be nearly eliminated by using FEM simulations instead of an analytical model (68). Garnett et al. (30) used capacitance-voltage (C-V) measurements to extract the radial carrier concentration profile and surface state density of individual silicon nanowires (**Figure 4**), which agreed well with diffusion simulations, planar control samples, and literature values for the surface state density. This result is encouraging because it means that with proper surface passivation, nanowire solar cells should be able to reach the same low level of surface recombination (per unit area) as planar cells. However, this result also suggests that unpassivated nanowires with diameters of less than 100 nm and doping levels near 1×10^{17} cm^{-3} can easily be completely depleted by the surface states (69). This is something that must be considered—the ungated conductivity measurement may be sampling only a small fraction of the nanowire volume and can thus result in errors in the carrier concentration, even when calculated using the correct mobility. Additionally, if there is a substantial dopant distribution within the nanowire, a single carrier concentration value gives only an estimate of the average value.

Although the C-V measurements mentioned above extracted the radial carrier concentration profile, they could not ascertain the dopant distribution directly. Perea et al. (29) used local electrode atom probe (LEAP) microscopy to see a nonuniform radial dopant profile for in situ–doped nanowires. **Figure 5** shows the enhanced surface dopant concentration and a schematic of the
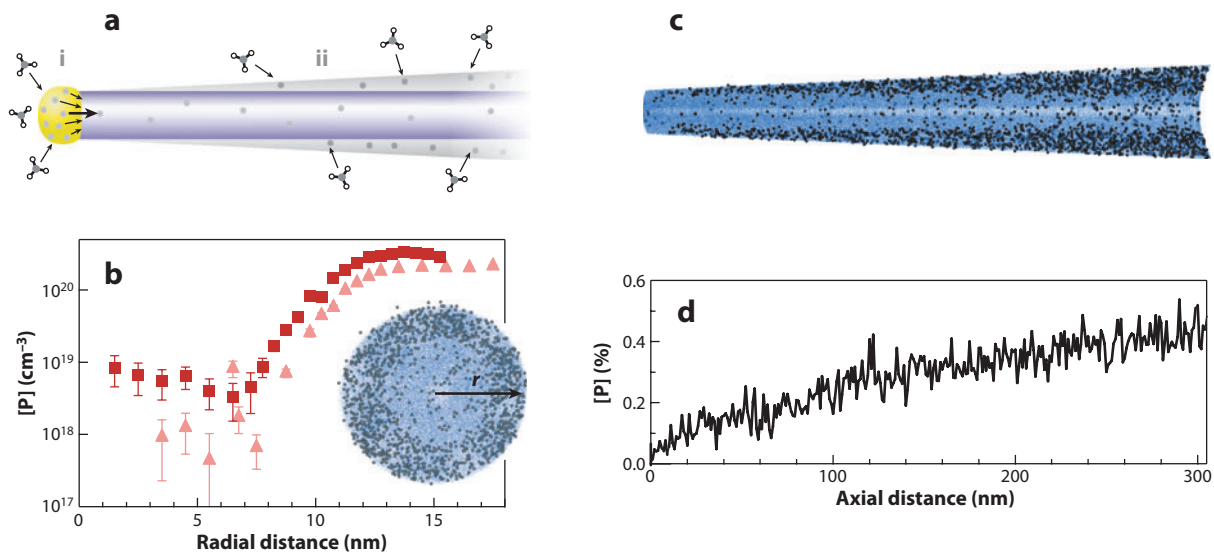

Figure 5

Distribution of dopant atoms and dopant incorporation pathways. (*a*) Schematic representation of dopant incorporation pathways via (*i*) the catalyst and (*ii*) the surface decomposition. (*b*) Radial plot of phosphorus concentration for germanium nanowires grown at 380°C and PH$_3$:GeH$_4$ ratios of 1:1,000 (*triangles*) and 1:500 (*squares*). The inset shows the path *r* along which the concentration was measured. (*c*) Side view of the nanowire cross section (2 nm thick) aligned with panel *d*. (*d*) Average phosphorus concentration [P] along the growth axis. Adapted with permission from Reference 29. Copyright © 2009, Macmillan.

proposed mechanism whereby phosphorus incorporates more efficiently through the uncatalyzed radial growth than through the catalyst. Koren et al. (70) used Kelvin probe force microscopy (KPFM) to demonstrate that even nanowires that did not show uncatalyzed radial growth (no tapering) had a 100-fold increase in phosphorus concentration at the surface compared with the core. This result underscores the potential errors involved in assuming uniform dopant distributions and ignoring surface state densities.

In addition to dopant profiling, catalyst incorporation into nanowires during growth is also of great concern, especially when metals that form deep traps (e.g., gold in silicon) are used. LEAP microscopy and high-angle annular dark-field (HAADF) imaging have shown that gold can dissolve into nanowires at concentrations between 1 ppm (roughly 1×10^{16} cm^{-3}) and 1×10^{20} cm^{-3} at growth temperatures below 500°C (71–73). There are some conflicting data regarding whether the gold segregates to the surface or has a uniform distribution throughout, which may be related to different growth conditions and material systems (71–73). Quantum-confined silicon nanowires synthesized using a titanium silicide catalyst showed substantial photoluminescence, whereas those catalyzed by gold did not, indicating that alternative catalysts can reduce metal-induced recombination (74).

Recombination through metal defects is not the only mechanism to reduce the minority carrier diffusion length in nanowire solar cells. Allen et al. (71) made single silicon nanowire solar cells by using one Schottky (gold) and one ohmic (nickel) contact on n-type wires patterned by e-beam lithography (**Figure 6**). E-beam-induced current (EBIC) measurements showed that the minority carrier diffusion length is strongly correlated with nanowire diameter, suggesting that surface recombination is the dominant factor (71). This recombination may stem from surface states but may also be caused by gold- or phosphorus-rich regions near the surface. Another study that also analyzed single silicon nanowire and microwire solar cells with scanning photocurrent spectroscopy found a minority carrier diffusion length of approximately two to four times the wire diameter (75). Calculations assuming that the minority carrier diffusion length was limited by the surface gave recombination velocities of 1,350 cm s^{-1}, similar to bulk values for the native oxide/silicon interface (76).

A number of studies have examined how the surface affects other electrical properties such as mobility. Ford et al. (9) found a linear correlation between mobility and diameter in indium arsenide nanowires, in which the gate capacitance was measured directly to minimize errors. This correlation suggests that surface scattering plays a significant role in reducing mobility and that surface passivation may help reduce this loss. Haick et al. (77) found an order-of-magnitude increase in silicon nanowire mobility after replacing the native oxide surface with a methyl-terminated surface, which reduces the surface recombination velocity by several orders of magnitude in silicon single crystals. The passivated nanowires showed mobility values comparable to those of bulk single crystals (78). Zhang et al. (79) also showed that surface states play a dominant role in the electrical properties of germanium nanowires. Demichel et al. (80) used an optical technique that they developed to measure surface recombination velocities of silicon nanowires after standard thermal oxidation and forming gas annealing passivation treatments. These latter researchers found values as low as 20 cm s^{-1}, similar to values for thermally oxidized silicon (100) (80). Assuming that the diode saturation current density is linearly proportional to surface recombination (which scales linearly with surface area and surface recombination velocity), we can expect a 60-mV decrease in V_{oc} for every order-of-magnitude increase in surface area, which is consistent with the experimentally observed and simulated results for high-purity silicon (11, 81). The above experimental evidence suggests that if properly implemented, surface passivation schemes already established for bulk semiconductors can limit detrimental surface effects in nanowire solar cells to a 10–15% efficiency loss compared with planar cells.
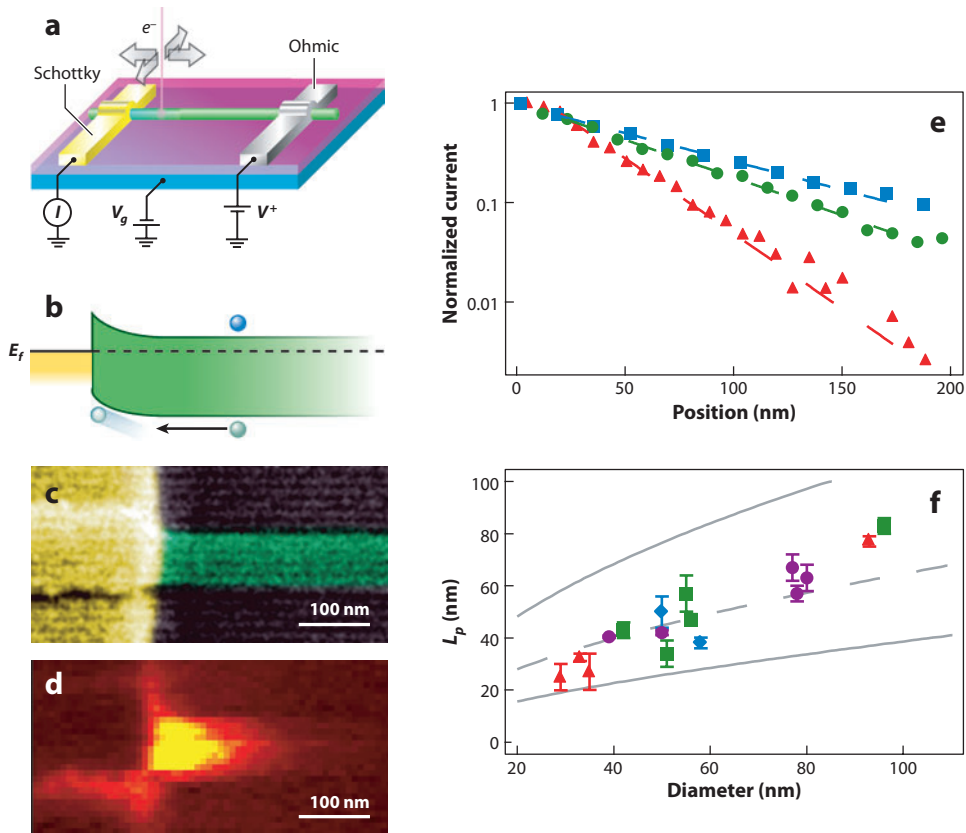
Figure 6

E-beam-induced current (EBIC) measurement on silicon nanowire devices and dependency on the diameter of minority carrier diffusion length. (*a*) Schematic of device geometry. (*b*) Band diagram near the Schottky contact. The Schottky junction between gold and *n*-type silicon separates minority (hole) and majority (electron) carriers to provide the photovoltaic effect. The gradient shading represents the relative probability of carrier collection. E_f is the Fermi energy. (*c,d*) False-color scanning electron microscopy image of a nanowire Schottky contact (*c*) and the EBIC image (*d*) taken simultaneously under a reverse bias of 0.3 V. (*e*) Semilogarithmic plot of EBIC profiles for nanowires having diameters of 93 nm (*blue squares*), 55 nm (*green circles*), and 35 nm (*red triangles*) with minority carrier diffusion lengths of 78 nm, 57 nm, and 28 nm, respectively. The dashed lines are fits to the current along the wire, which decays as ae^{-x/L_p}, where L_p is the minority carrier diffusion length. (*f*) Plot of L_p versus diameter for varying gas-phase Si:P doping ratios: 500:1 (*red triangles*), 1,000:1 (*green squares*), 1,500:1 (*blue diamonds*), and 2,000:1 (*purple circles*). Gray lines are model calculations of L_p versus nanowire diameter for various values of the surface recombination velocity S. Top, bottom, and dashed lines correspond to $S = 1 \times 10^5$ cm s^{-1}, 1×10^6 cm s^{-1}, and 3×10^5 cm s^{-1}, respectively. Adapted with permission from Reference 71. Copyright © 2008, Macmillan.

Nanowire solar cell absorption, charge transfer, and carrier collection efficiency can be measured using standard techniques for bulk solar cells. The results and benefits are discussed in the next section.

3. BENEFITS OF THE NANOWIRE GEOMETRY

In any solar cell, there are many sources of loss that must be minimized. The steps required to convert light to electricity are photon absorption, exciton creation, exciton separation to free carriers,

and carrier collection by the electrodes. Using nanowires instead of wafers or thin films provides opportunities to minimize losses in each step at lower costs. The potential cost benefits come primarily from lowering the purity standard and the amount of semiconductor material needed to obtain high efficiencies; increasing the defect tolerance; and enabling new single-crystalline materials to be used without expensive, lattice-matched substrates. The major benefits associated with each photoconversion step are depicted in **Figure 1** and are described in detail below.

3.1. Absorption

Absorption losses can be divided into two categories: reflection, in which not all of the light is able to enter the semiconductor, and transmission, in which the sample either is too thin or does not have sufficient light trapping to quench all the photons. Antireflection coatings address the first loss, whereas light-trapping schemes affect the second loss. Although both antireflection and light-trapping schemes improve absorption, it is important to differentiate between the two mechanisms to understand how photocurrent can be increased for different solar cell structures.

Reflection at an interface arises from a difference in refractive index between two media (82). In the case in which there is no antireflection coating, most inorganic semiconductors will reflect between 10% and 50% of the light in the range of 400 to 2,000 nm, where most of the sun's power lies. For example, a silicon solar cell without an antireflection coating will lose more than 30% of its power to reflection (51). One common strategy to reduce reflection is to add one or more coatings that have a refractive index intermediate between that of the semiconductor and that of air (83). Using an appropriate coating thickness and refractive index leads to destructive interference between reflected light and incident light, eliminating reflection at both interfaces. Unfortunately, this technique is completely effective only for a single wavelength at normal incidence, so there will still be some reflectance over most of the spectrum. Double- and triple-layer coatings can spectrally broaden the response, but the ideal coating would have a continuously graded refractive index. Tapered nanowire arrays (nanocones) with tips much smaller than the wavelength of light act as an effective medium, with a gradual change in refractive index given by the weighted average of the material and air. **Figure 7** shows that this approach leads to greatly enhanced absorption compared with planar samples over a broad wavelength and angle range (84). Nanocones show improved performance over both nanowires and thin films. Because all the amorphous silicon (a-Si) films in this study were optically thick (i.e., thick enough that there is no transmission) over the wavelength range measured, the increased absorption can be attributed to reduced reflection and does not provide information on light-trapping effects. Other studies have also reported greatly reduced reflection with tapered and untapered nanowires made of different materials, including crystalline silicon, gallium nitride, indium phosphide, gallium phosphide, germanium, and cadmium sulfide (14, 85–88).

Although the antireflection properties of nanowire arrays have been extensively studied for a broad range of materials and morphologies, as mentioned above, most of these reports did not investigate light-trapping effects. Light-trapping schemes have been implemented in commercial wafer-based and thin-film solar cells and usually involve creation of random surface texturing (51, 78). Yablonovitch & Cody (89), using statistical mechanics and geometrical optics approaches, first derived the limit of a perfectly implemented randomized (i.e., Lambertian) light-trapping scheme. Both methods showed a maximum light intensity enhancement within the medium of $2n^2$ compared with the incident beam, where n is the refractive index of the medium. This corresponds to a path length enhancement of $4n^2$ ($\sim$50 for silicon, depending on wavelength) when angle averaging is considered. The only assumptions in this derivation are that the medium does not absorb light (a good approximation for the very weak absorption limit) and that the light is
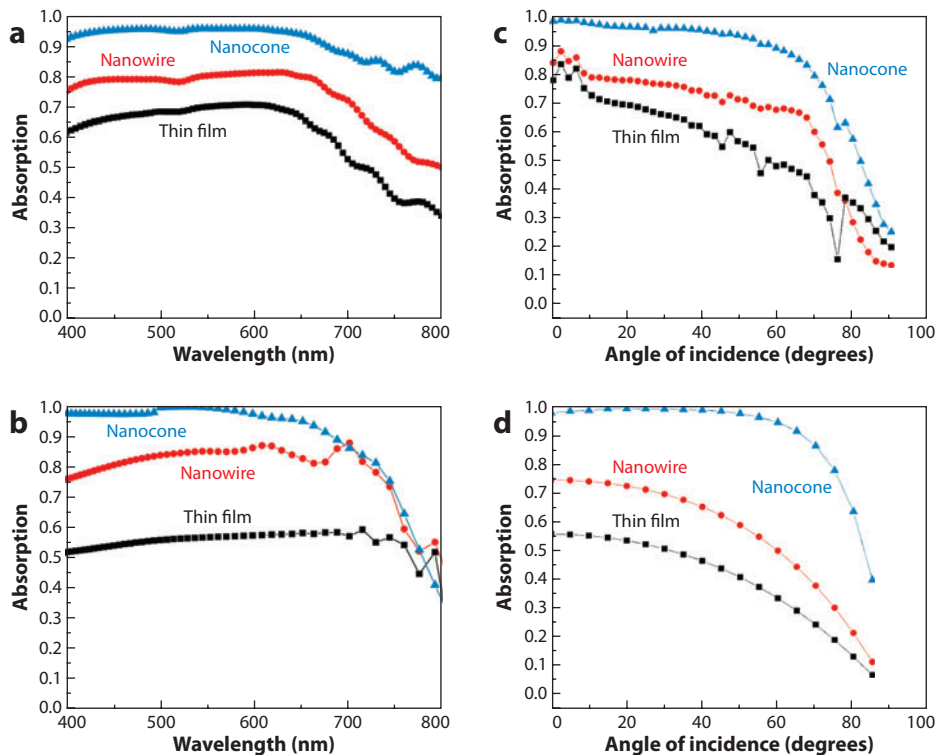
Figure 7

Antireflection properties of nanowires and nanocones. (*a*) Measured and (*b*) simulated values of absorption on samples with amorphous Si:H (a-Si:H) thin films, nanowire arrays, and nanocone arrays over a large range of wavelengths at normal incidence. (*c*) Measured and (*d*) calculated values of absorption on samples with a-Si:H thin films, nanowire arrays, and nanocone arrays over different angles of incidence (at wavelength $\lambda = 488$ nm). Adapted with permission from Reference 84. Copyright © 2009, American Chemical Society.

completely randomized once it enters the structure. According to these two assumptions, a random array of nanowires may still be held to the $4n^2$ limit, but a periodic array should be able to exceed it. Muskens et al. (90) used enhanced backscattering spectroscopy to demonstrate that random arrays of gallium phosphide nanowires act as strong scattering centers, with optical mean free paths as low as 160 nm. The optical mean free path, defined as the average distance that light travels in the array between nanowire scattering events, decreased with increasing photon energy, and the diameter-dependent shift in the spectral response curves was attributed to optical resonances along the nanowire diameter. This resonance effect was much stronger for arrays grown on (100) substrates, in which the nanowires grew along several off-vertical directions, than for arrays grown on (111)B substrates, in which all the nanowires were vertically oriented. This is not surprising, considering that diameter-dependent resonances can be excited only by scattered light in vertical nanowire arrays but the resonances can be excited directly by the incident beam in angled nanowires. Cao et al. (7, 91–93) studied these leaky-mode resonances, which resemble a whispering gallery mode in a microdisk cavity, in greater detail by measuring the photocurrent and scattering spectrum of single nanowires lying flat on a substrate (**Figure 8**). They found a redshift in the scattering and absorption efficiency peaks with increasing diameter and matched the experimental data to Lorentz-Mie scattering calculations and finite difference time domain simulations
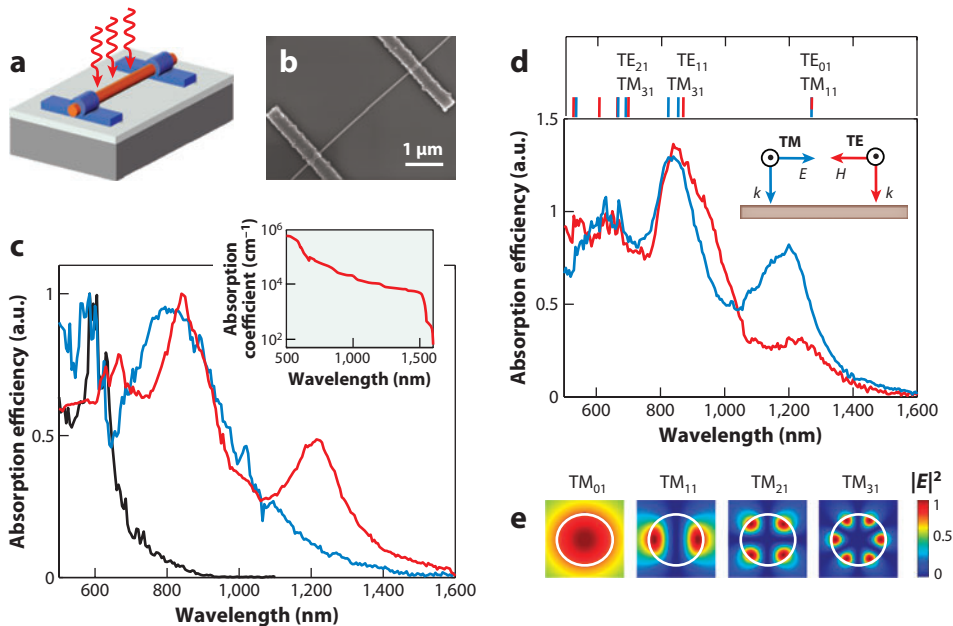
Figure 8

Measurement of light absorption in individual germanium nanowire devices and correlation of the absorption peaks with leaky-mode resonances (LMRs). (*a*) Schematic illustration of the germanium nanowire device used for photocurrent measurements. (*b*) Scanning electron microscopy image of a 25-nm-radius germanium nanowire device. (*c*) Measured spectra of absorption efficiency Q_{abs} for unpolarized light taken from individual germanium nanowires with radii of 10 nm (*black*), 25 nm (*blue*), and 110 nm (*red*). The spectra are normalized to their maximum absorption efficiency to highlight the tunability of the nanowire absorption properties. (*Inset*) Absorption coefficient of bulk germanium as a function of wavelength. (*d*) Q_{abs} spectra of a 110-nm-radius germanium nanowire taken using linearly polarized transverse-electric (TE; *red*) or transverse-magnetic (TM; *blue*) light. The spectra are normalized to an internal quantum efficiency of four, which is assumed to yield the best fit between the calculated and experimental results. The inset illustrates the illumination geometry for the TE (the electric field of the light polarized perpendicular to the axis of the wire) and TM (the electric field of the light polarized parallel to the axis of the wire) polarizations. The red/blue lines at the top indicate locations of all LMRs of the 110-nm-radius germanium nanowire in this spectral region. Only some of the modes are labeled for visualization convenience. *E*, *H*, and *k* are the electric field, magnetic field, and *k* vector of the incoming light, respectively. (*e*) The configuration of the electric field intensity for typical TM leaky modes. The white circle denotes the nanowire/air interface. Adapted from Reference 91.

(7, 91–93). The simulated field plots showed distinct resonant modes at spectral peaks, as expected. The absorption efficiency decreased as the incident angle moved away from the normal direction, again confirming that these leaky-mode resonances are the dominant light-trapping effect in single nanowires or arrays of horizontal nanowires. In addition to exciting resonances that can increase absorption, single nanowires can also show improvements in absorption with less material by offering an enhanced optical cross section over the geometrical cross section. The exceptionally high current observed by Tian et al. (47) for individual silicon nanowire solar cells lying on a substrate certainly had contributions from these resonance and optical cross-section effects in addition to the increased absorption coefficient in nanocrystalline silicon, the latter of which was given as an explanation.

In addition to the scattering, resonance, and increased effective optical cross-section benefits that single nanowires and random arrays offer, ordered arrays can also benefit from diffraction effects, collective resonances, and changes in the optical density of states. Such ordered structures may not be bound by the randomized scattering limit. Garnett & Yang (11) measured the photocurrent of solar cells made with the same ordered silicon nanowire array but different silicon absorber thicknesses to determine the light-trapping path length enhancement factor. These researchers repeated the light-trapping measurements using arrays with different lengths and found a strong increase in path length enhancement factor with nanowire length (**Figure 9**). The path length enhancement factor is defined as the apparent optical thickness of the structure divided by its actual thickness. The roughness factor in **Figure 9** is defined as the ratio between the nanowire array surface area and the geometric surface area (surface area of a planar control). The strong correlation between path length enhancement and roughness factor (proportional to nanowire length) is especially striking; because the nanowires were formed by etching, the increased length significantly reduced the amount of silicon available for absorption. The best nanowire arrays showed path length enhancement factors of up to 73, exceeding the randomized scattering limit ($2n^2 \sim 25$ because there was no back reflector). Optical transmission measurements corroborated the photocurrent data. The strong dependency on nanowire length may come from inefficient coupling to photonic crystal and waveguiding modes for short nanowires, but full-field optical simulations will be necessary to understand this phenomenon completely. Zhu et al. (94) performed optical simulations showing that periodic semiconducting nanocones with aspect ratios approaching 1 can effectively couple light into waveguiding modes within an a-Si solar cell. Their absorption measurements showed strong enhancements that agreed with the simulations, and the nanostructured solar cells showed a more-than-50% increase in short-circuit photocurrent density over planar control cells. The exceptional J_{sc} of 17.5 mA cm^{-2} is above that of the world record a-Si solar cell, although the efficiency is much lower due to V_{oc} and FF losses (95). Kelzenberg et al. (96) also found absorption enhancements above the randomized scattering limit in periodic arrays of silicon microwires, although the length, diameter, and filling fraction were nearly an order of magnitude different (far from subwavelength), so the enhancement mechanisms may not be the same. A number of other papers reporting periodic arrays of cadmium telluride and dual-diameter germanium nanowires made by templated chemical vapor deposition likely also show enhanced absorption due to the periodicity, although such papers do not include the analysis or enough data to calculate the enhancement factor (14, 88).

Finally, nanowires can show increased absorption via resonant energy transfer from dyes or quantum dots located near the semiconductor surface. Because of the larger surface area compared with planar samples, this energy transfer can substantially affect absorption (**Figure 10**). Peters et al. (97) demonstrated theoretically that silicon nanowires only 7 μm long and 50 nm in diameter can absorb 84% of the above band gap radiation with the help of a surface dye compared with only 56% without the dye. These calculations did not consider any of the light-trapping effects described above, which will increase absorption both with and without the dyes, although the relative enhancement is unknown. Using nanowires with optical resonances located at the dye absorption peak may amplify the energy transfer effect by increasing the electric field at the surface. Experimentally, Lu et al. (98) used time-resolved photocurrent measurements to show that lead sulfide nanocrystals can resonantly transfer energy to silicon nanowires. These investigators showed a strong correlation between the photoluminescence spectrum of lead sulfide quantum dots and the time-integrated photocurrent enhancement, as predicted by the transfer efficiency equations. Considering the conflicting factors of increased surface recombination and light-trapping effectiveness for longer nanowires, surface modification with dyes may help to optimize overall performance in nanowire solar cells.
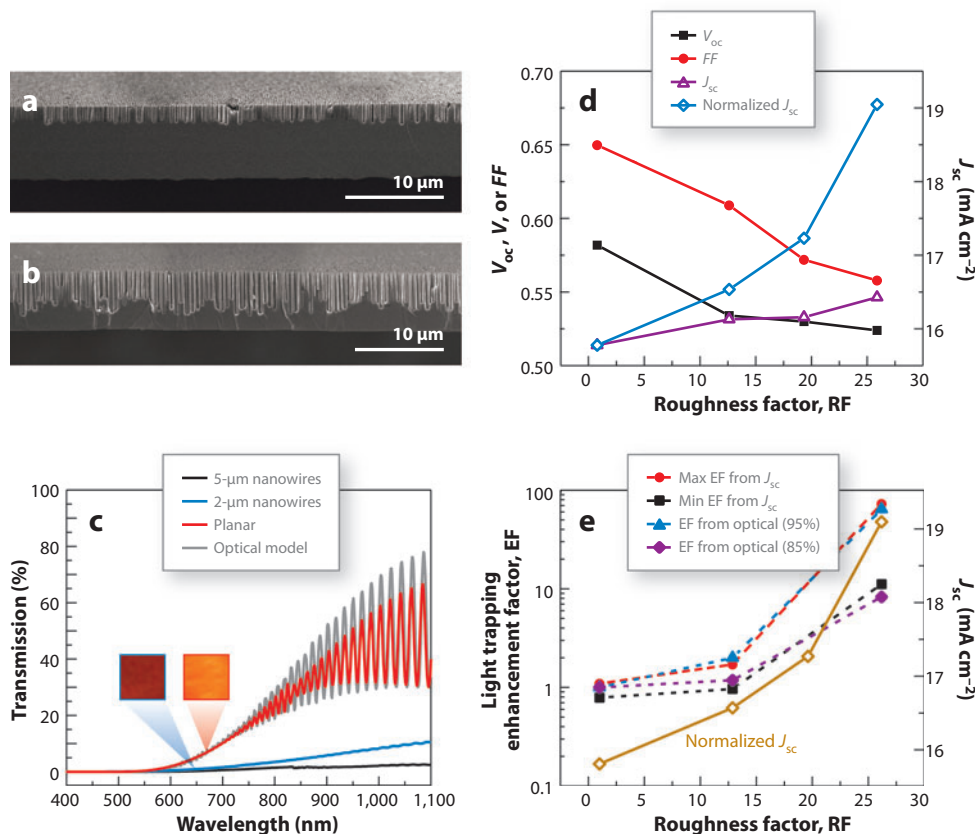
Figure 9

Optical transmission measurements on thin silicon windows with and without nanowires, photovoltaic response, and light-trapping effect as a function of roughness factor (RF). RF is defined as the ratio between nanowire array surface area and planar control surface area, which scales with nanowire length. Tilted cross-sectional scanning electron microscope images of (*a*) 2-μm nanowire arrays and (*b*) 5-μm nanowire arrays etched into 7.5-μm-thick silicon windows. (*c*) Transmission spectra of thin silicon window structures before etching (*red*) and after etching to form 2-μm (*blue*) and 5-μm (*black*) nanowires. The spectrum from an optical model for a 7.5-μm-thick silicon window (*gray*) matches very well with the planar control measurement. The insets are backlit color images of the membranes before and after etching. There is a large intensity reduction and redshift in the transmitted light after the nanowires are formed, suggesting strong light trapping. (*d*) The V_{oc}, *FF*, and J_{sc} of periodic silicon nanowire array solar cells fabricated from an 8-μm-thick silicon absorber with three different RFs compared with a planar control (RF = 1). The normalized J_{sc} is determined by dividing the nanowire J_{sc} by the fraction of light that should be absorbed compared with the planar control, considering the loss in silicon volume for the nanowire cells. The increasing J_{sc} with higher RF suggests that the light-trapping effect induced by ordered nanowire arrays is sufficient to overcome the increased surface and junction recombination that comes with longer nanowires. (*e*) Light-trapping path length enhancement factor (EF) versus RF on a semilog scale derived by comparing the J_{sc} from ordered silicon nanowire arrays with the same RF but different absorber thicknesses (*red* and *black*) and from the optical transmission measurements in panel *c*, assuming that 95% (*blue*) or 85% (*purple*) of the reduced transmission ultimately leads to absorption. The normalized J_{sc} (*gold*) is also shown on a linear scale for comparison. The strong correlation further supports the light-trapping effect because absorption (and ultimately photocurrent) scales with the logarithm of the path length. Adapted with permission from Reference 11. Copyright © 2010, American Chemical Society.
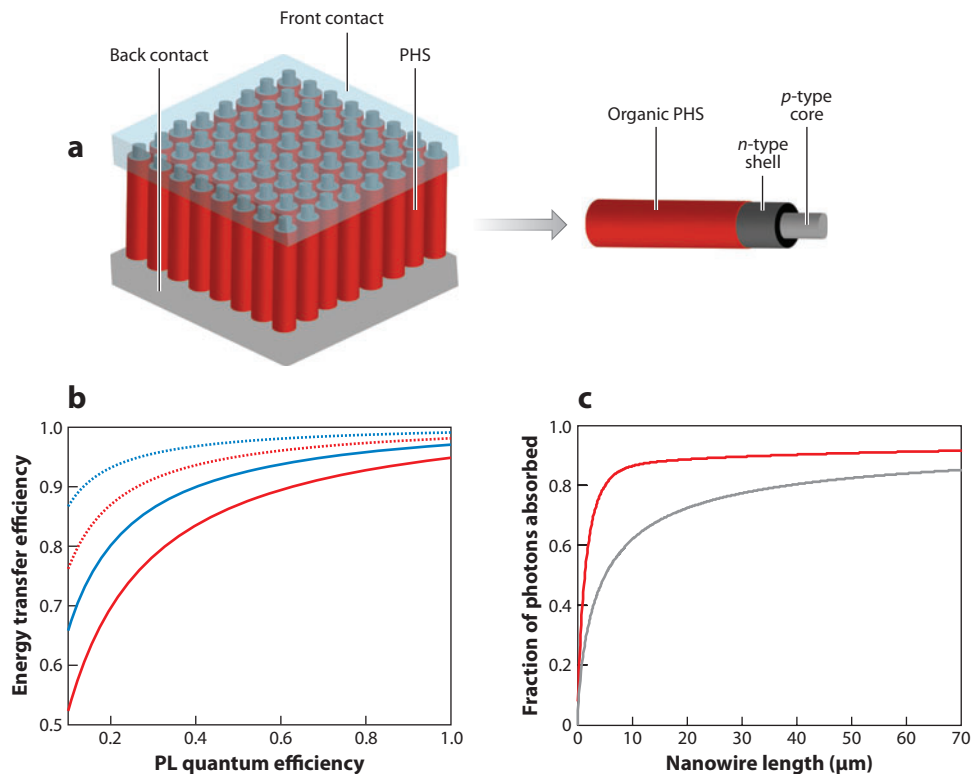
Figure 10

Increasing light absorption in nanowires through resonant energy transfer from photon-harvesting shells (PHS). (*a*) Schematic of a nanowire solar cell with a PHS. Organic molecules are chemically attached to the surface of the nanowires. The organic shell absorbs light and transfers the energy to the silicon nanowires via resonant energy transfer. The silicon nanowires have radial *p-n* junctions that selectively separate and transport the charges to the respective electrodes (shown in the isolated nanowire to the *right*). (*b*) Energy transfer efficiency (ETE) as a function of dye photoluminescence (PL) efficiency for dye A (*blue*) and dye B (*red*). The solid and dashed lines are for x values of 2.7 nm and 1.7 nm, respectively, where x is the dye separation distance from the nanowire surface. The much weaker variation of the dashed curves compared with the solid curves shows that it is important to carefully control the dye-silicon separation to achieve a high ETE for arbitrary dyes. (*c*) Fractions of photons above the band gap of silicon that are absorbed with bare silicon nanowires (*gray*) and with dyes A and B attached to the nanowires (*red*) as a function of nanowire length. The nanowires are 50 nm in diameter, with a center-to-center distance of 70 nm. Dyes A and B are assumed to have equal surface coverage with a molar absorptivity of 2×10^5 M^{-1} cm^{-1} and surface concentration on the wires of 7.5×10^{13} cm^{-2}. Adapted with permission from Reference 97. Copyright © 2009, American Institute of Physics.

3.2. Exciton Formation

After light is absorbed in the solar cell, the next loss mechanism is carrier relaxation. If the exciton binding energy is weak compared with the available thermal energy at room temperature (e.g., in bulk silicon), the excited carriers will relax to the band edge as free carriers. If the exciton binding energy is strong (as in most organic semiconductors), the carriers will form a bound exciton state. This carrier relaxation normally occurs by carrier-phonon coupling such that the energy is lost as heat. This is the single greatest loss mechanism in every photovoltaic device and typically represents between 30% and 40% of the incident solar energy (1). The simplest way to reduce heat losses is

to choose a material with an optimal band gap or several materials with optimal complementary band gaps for single-junction and multijunction solar cells, respectively. One method commonly used to adjust material band gaps is to alloy multiple materials together. However, some common alloys, such as indium gallium nitride, show a miscibility gap at intermediate concentrations caused by large lattice mismatch strain, which makes it difficult to synthesize uniform single-crystalline films at arbitrary compositions. Nanowires close this miscibility gap by providing improved strain relaxation, opening up a broader range of absorption energies than is possible with thin-film materials (99). Additional tuning can come from reducing the nanowire diameter to near or below the Bohr radius of the material, when quantum confinement begins to cause an increase in band gap (100). This is practically useful only in materials with large Bohr radii and relatively small starting band gaps, such as germanium and lead selenide. Another strategy to reduce heat loss is to introduce some nonlinear carrier generation scheme such as multiple exciton generation (MEG) (1). Quantum confined systems also exhibit greatly enhanced MEG yield (101, 102). The enhancement mechanism is still under debate, but proposed mechanisms include reduced electron-phonon coupling, relaxed momentum conservation, and enhanced Auger processes in quantum confined systems, all of which would increase the probability of the desired MEG relaxation pathway over standard thermalization.

3.3. Charge Separation

Nanowires also provide an opportunity to use new charge separation mechanisms. Wu et al. (100) used density functional theory to show that tapered nanowires that exhibit different degrees of quantum confinement along the length can separate electrons and holes without any dopants. **Figure 11** shows the spatial separation between the highest occupied molecular orbital (HOMO) and the lowest unoccupied molecular orbital (LUMO) wave functions in a tapered quantum silicon nanowire, leading to a spontaneous potential gradient. In another theory paper, the same authors showed that a change in band gap induced by varying strain along the nanowire length can also be used to separate charges in a similar manner (103). It is unclear if such a material would have the same V_{oc} and FF limitations as traditional cells, which warrants further study. This exciting new charge separation mechanism has yet to be realized experimentally, but it opens up the possibility of making a solar cell from undoped materials with very low Auger recombination rates, which is often the limiting factor in high-efficiency solar cells (51, 78, 104).

3.4. Carrier Collection

Once carriers have been separated, they must diffuse to the contacts to be extracted for useful work. The nanowire geometry is especially beneficial for this step because it enables rapid radial charge separation and efficient carrier collection through band conduction (81). Law et al. (12) demonstrated such a scheme, using zinc oxide nanowires in a dye-sensitized solar cell. They showed that the carrier collection efficiency is much higher for the nanowire case compared with the standard nanoparticle case due to faster band conduction rather than a trap-limited diffusion transport mechanism. Later papers based on this principle showed substantial efficiency improvements by using titania shells to reduce surface recombination rates or titania nanotubes to increase the total surface area (17, 63). Despite this improved transport, the nanowire dye-sensitized solar cells have still not been able to match the nanoparticle cell performance due to the lower surface area (and thus lower dye loading). A much shorter zinc oxide nanowire network also showed improved charge transport in inverted polymer bulk heterojunction solar cells compared with controls on planar zinc oxide films manifested in higher FF and overall efficiency
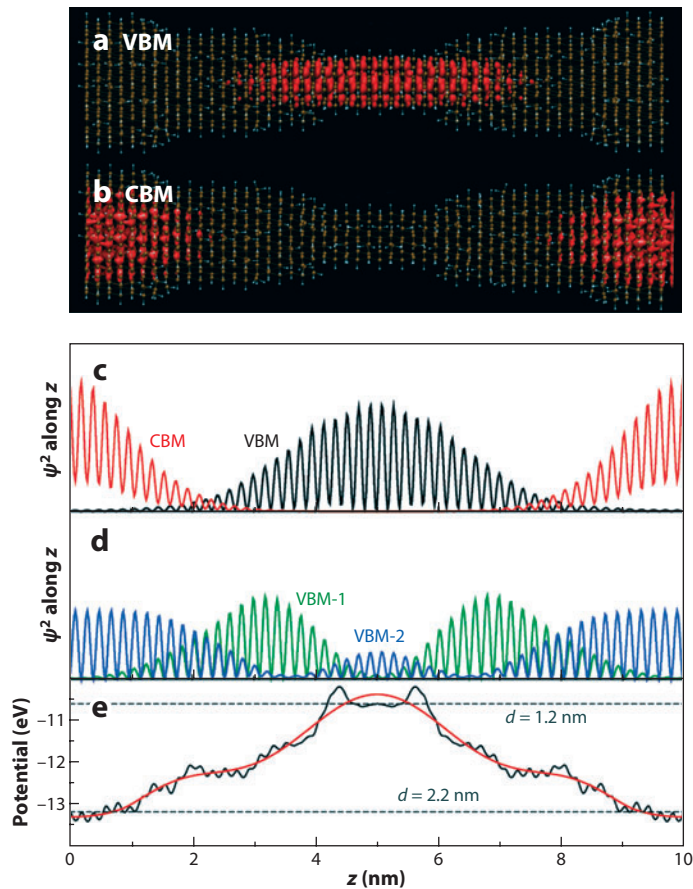
Figure 11

Charge separation using quantum confinement. Panels *a* and *b* show isosurfaces (*red*) of the square of the wave functions of the valence band maximum (VBM) and conduction band minimum (CBM) in the tapered nanowires at values of 10% of their respective maximum. Panels *c* and *d* show the charge density distribution of the VBM, CBM, VBM-1, and VBM-2 states along the wire axis (integrated over the *xy* plane). Panel *e* shows the planar-averaged total potential $V(z)$ along the wire axis for the tapered nanowires (*solid black*) and the straight-edged nanowires (*dashed black*). The red curve is a polynomial fit to the black solid curve. Adapted with permission from Reference 100. Copyright © 2008, American Physical Society.

(22, 105). Considering the light-trapping discussion above, ordered nanowire arrays may be able to provide additional gains in efficiency by improving absorption in both dye-sensitized and bulk heterojunction polymer solar cells.

Another advantage of the radial junction is the decreased sensitivity to bulk defects. Kayes et al. (81) predicted that silicon nano- or microwires with radial *p-n* junctions should show only a slight efficiency degradation with decreasing lifetime until the minority carrier diffusion length approaches the nanowire radius, whereas planar *p-n* junction cells show severe degradation once the diffusion length drops below the film thickness. **Figure 12** shows that this effect is strongest when there is a large mismatch between the absorption and minority carrier diffusion lengths, which is more likely to occur in indirect band gap semiconductors like silicon than in direct band gap materials like gallium arsenide. One important and often overlooked caveat to these results is that the radial junction solar cells show an efficiency advantage primarily when the defects
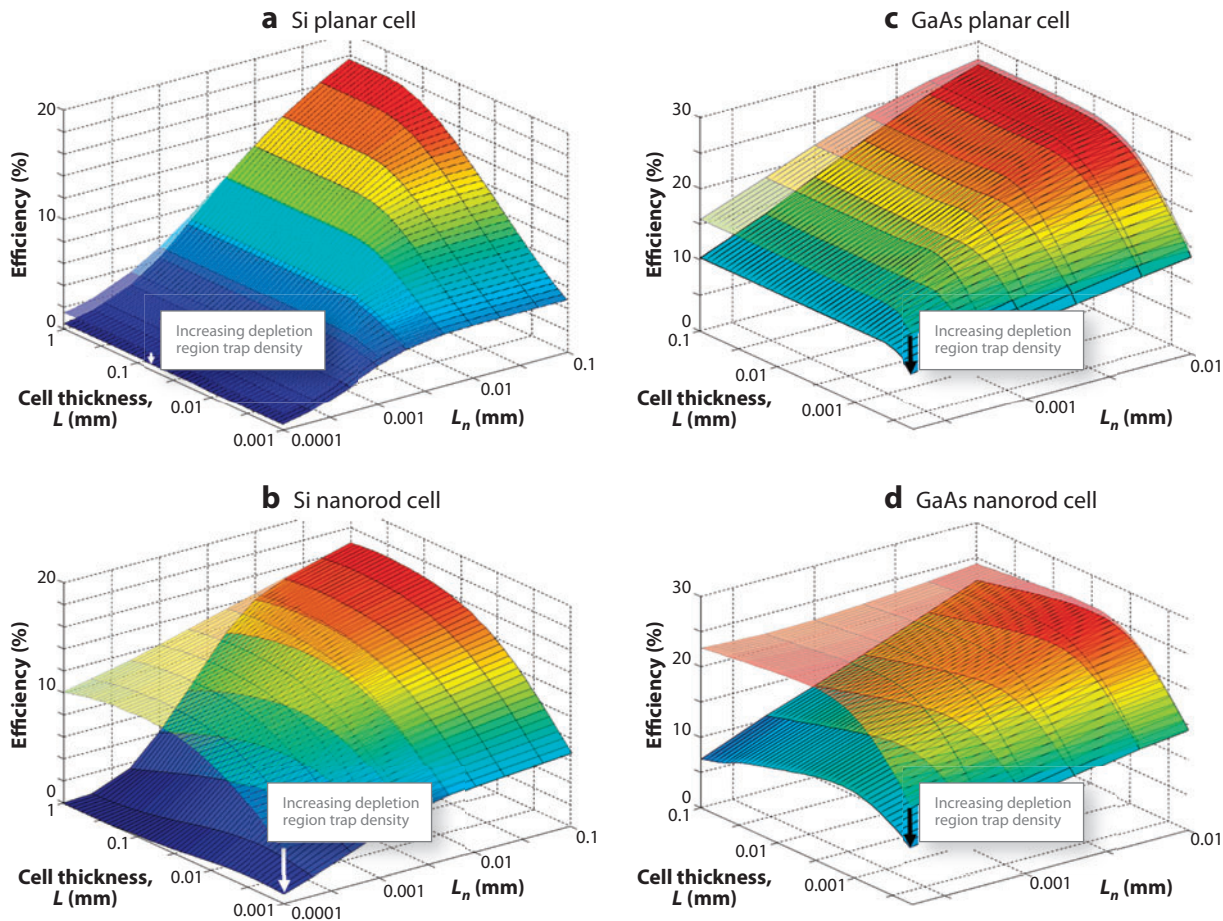
a Si planar cell

c GaAs planar cell

b Si nanorod cell

d GaAs nanorod cell

Figure 12

Efficiency versus cell thickness L and minority electron diffusion length L_n for (*a*) a conventional planar *p-n* junction silicon cell, (*b*) a radial *p-n* junction nanorod silicon cell, (*c*) a conventional planar *p-n* junction gallium arsenide (GaAs) cell, and (*d*) a radial *p-n* junction nanorod GaAs cell. In all cases the top surface shown in the plot has a depletion region trap density fixed at 10^{14} cm^{-3} so that the carrier lifetimes τ_{n0}, $\tau_{p0} = 1$ μs, whereas the bottom surface has a depletion region trap density equal to the trap density in the quasi-neutral region at each value of L_n. In the radial *p-n* junction nanorod case, the cell radius R is set equal to L_n, a condition that is near optimal. Adapted with permission from Reference 81. Copyright © 2005, American Institute of Physics.

are concentrated in the quasi-neutral region of the device (the upper surfaces in the **Figure 12** plots); high defect densities in the depletion region degrade performance significantly for both planar and radial junctions (the lower surfaces in the **Figure 12** plots). Verifying the benefits of the radial geometry requires some control over the minority carrier diffusion length or carrier extraction length in nanowire cells. Single-nanowire solar cell measurements showed an efficiency increase of approximately a factor of five for radial versus axial *p-n* junctions, due primarily to an improved photocurrent (**Figure 13**) (47, 106). It is tempting to assume that the increased efficiency (and photocurrent) stems from improved minority carrier collection in the radial geometry. However, even in the axial *p-n* junction study, the photocurrent increased linearly with the active area (the intrinsic nanowire length), contrary to what would be expected if charge separation and carrier collection were limiting performance. The five-times-lower J_{sc} observed in the axial versus
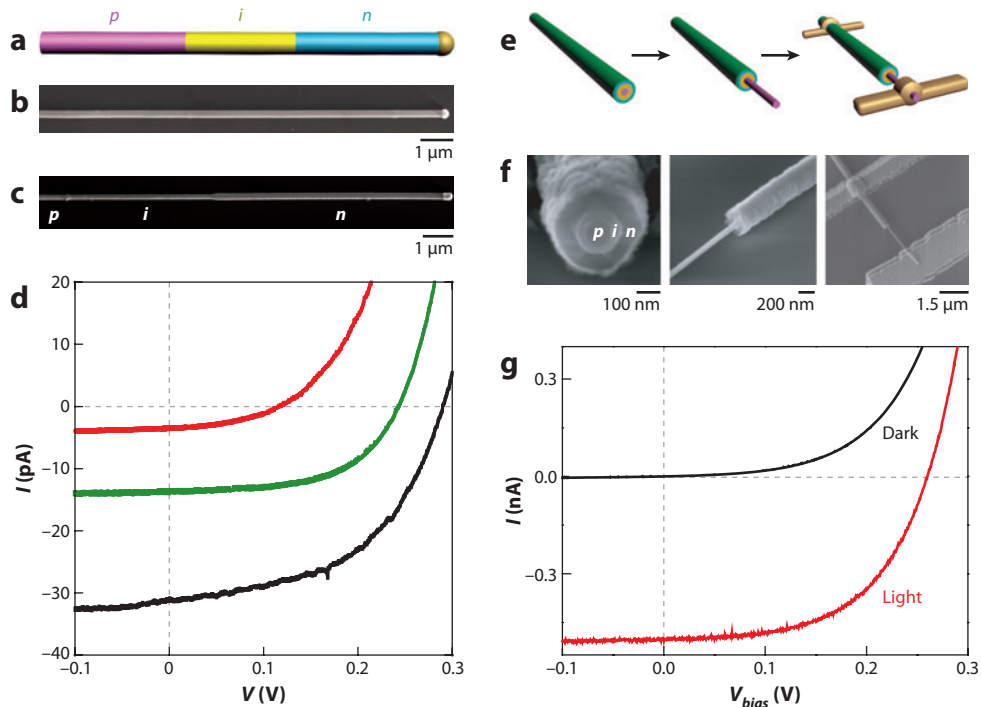
Figure 13

Axial and radial *p-i-n* silicon nanowire solar cells. (*a*) Schematic of an axially modulated *p-i-n* silicon
nanowire. Growth is mediated with a gold catalyst (gold-colored hemisphere) in a sequence beginning with
the *p* and *i* regions and ending with the *n* region. (*b*) Scanning electron microscopy (SEM) image of a
uniform *p-i-n* axial silicon nanowire with a gold catalyst (*d* = 250 nm) visible on the right end. (*c*) SEM
image of a *p-i-n* axial nanowire after selective wet etching. The *p*- and *i*-type silicon regions have faster
etching rates than the *n*-type region. (*d*) Light *I-V* characteristics for the *i* length = 0-, 2-, and 4-μm devices
(*red*, *green*, and *black*, respectively); the illumination intensity is 100 mW cm^{-2}, air-mass 1.5 global (AM 1.5)
spectrum. (*e*) Schematics of radial *p-i-n* junction device fabrication. (*Left*) Pink, yellow, cyan, and green layers
correspond to the *p* core, *i* shell, *n* shell, and plasma-enhanced chemical vapor deposition–coated silicon
dioxide, respectively. (*Middle*) Selective etching to expose the *p* core. (*Right*) Metal contacts deposited on the
p core and *n* shell. (*f*) SEM images corresponding to the schematics in panel *e*. (*g*) Dark and light *I-V* curves
of a typical radial *p-i-n* junction device. Panels *a–d* adapted with permission from Reference 106. Copyright
© 2008, American Chemical Society. Panels *e–g* adapted with permission from Reference 47. Copyright ©
2007, Macmillan.

radial nanowire *p-n* junction must come from differences in absorption, internal quantum effi-
ciency (IQE) (which measures charge separation and extraction efficiency), or some combination
of both. Considering that the extraordinarily high J_{sc} reported for the radial *p-n* junction study
(three times the expected value for single-pass absorption, assuming 100% IQE, with bulk ab-
sorption coefficients) was attributed to an increased absorption coefficient in the nanocrystalline
shell, whereas the axial nanowires were completely single crystalline, it is difficult to determine the
charge separation (IQE) benefit of the radial geometry from these studies without absorption sim-
ulations or measurements. An additional complicating factor is that the radial junction nanowires
had a significantly (almost twofold) larger diameter, possibly enabling higher-order leaky-mode
resonances to increase the absorption more than expected from a simple Beer's law calculation, as
observed experimentally and theoretically in germanium nanowires (7, 91, 92). These resonances,

which concentrate light near the outer diameter of the nanowire, should increase absorption even more when there is a highly absorbing shell, as in the radial *p-i-n* junction case (**Figure 13**).

The charge separation advantages of the radial geometry are more obvious in a paper from Fan et al. (14) that shows an increase in efficiency from approximately 0.5% to nearly 6% by increasing the interpenetration of cadmium sulfide nanowires into a constant-thickness cadmium telluride thin film. **Figure 14** indicates that the fraction of charges that can be removed from the device increases dramatically with nanopillar length, as expected when the minority carrier diffusion
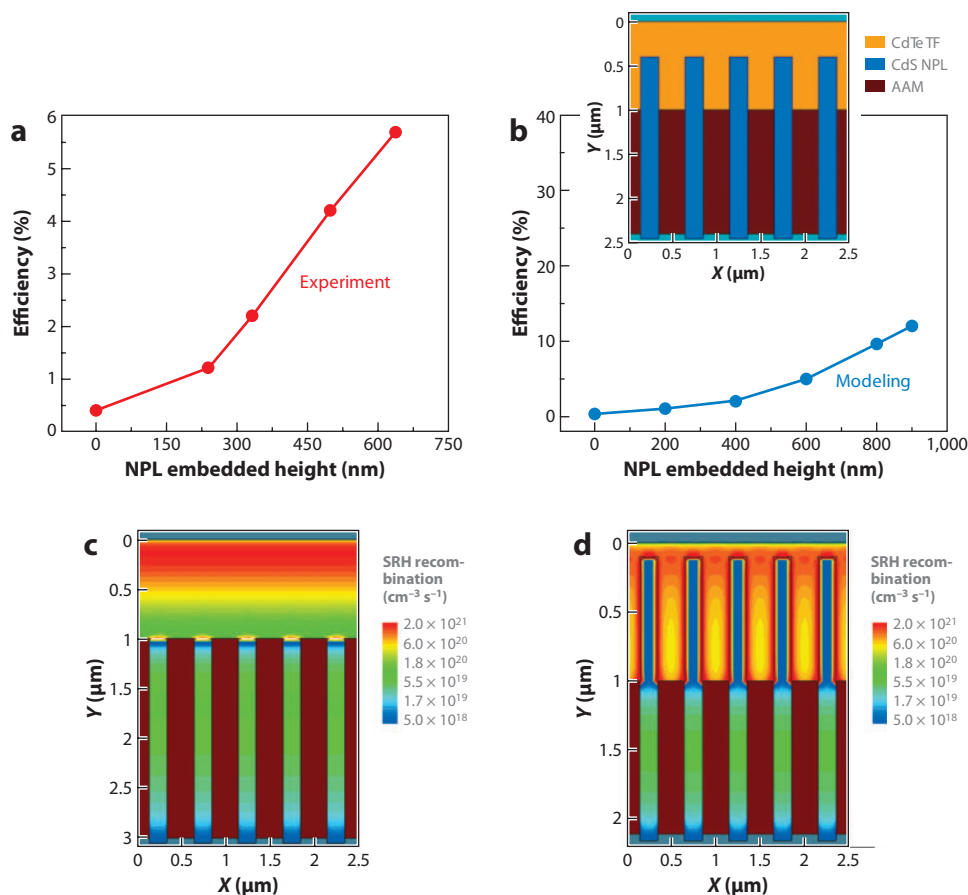

Figure 14

Effects of the nanopillar geometric configuration on device performance. (*a*) Experimentally obtained efficiency of solar nanopillar (SNOP) cells as a function of the embedded nanopillar height, *H*. The cadmium telluride film thickness is maintained constant at ~1 μm. (*b*) Theoretical simulation of the SNOP cell efficiency as a function of *H*, in qualitative agreement with the observed experimental trend shown in panel *a*. TF denotes thin film; NPL denotes nanopillar; and AAM denotes anodic alumina membrane, used for the NPL templating. (*Inset*) Schematic diagram of the SNOP cell used for the simulation. (*c,d*) Visualization of Shockley-Read-Hall (SRH) recombination in SNOP cells with (*c*) *H* = 0 nm and (*d*) *H* = 900 nm. The space charge and carrier collection region is quite small when *H* = 0 nm, resulting in a major carrier loss in the upper portion of the cadmium telluride film through recombination, where there is a high electron-hole pair (EHP) optical generation rate. However, the space charge and carrier collection region is significantly enlarged when *H* = 900 nm; thus, the total volumetric carrier recombination loss is greatly reduced. Adapted with permission from Reference 14. Copyright © 2009, Macmillan.

length is substantially smaller than the film thickness. The results are somewhat obscured by the possibility of improved absorption with longer nanopillars due to the periodic light-trapping effects described above. However, 1-μm cadmium telluride films already absorb a majority of the above band gap radiation, so optical effects alone cannot account for the order-of-magnitude efficiency improvement. Additionally, the longer nanopillars will have increased interface recombination, which will reduce the efficiency. Device physics simulations, which consider recombination but not light-trapping effects, qualitatively agree with the experimental results (**Figure 14**).

3.5. Cost

All the above benefits of the nanowire geometry promise to lower the cost of solar cells by reducing the amount of material needed (lower reflection, superior light trapping), by expanding the list of available materials (band gap tuning, new charge separation mechanisms), or by relaxing the materials purification requirements (enhanced charge separation in low-lifetime materials). But nanowires may also offer an enormous cost benefit for the fabrication steps of high-performance multijunction solar cells by removing the need for an expensive lattice-matched substrate. Many materials relevant to solar cells, including zinc oxide, germanium, silicon, indium gallium nitride, and cadmium sulfide, can be made into single-crystalline nanowires on nonepitaxial substrates through bottom-up synthesis, with some grown directly on electrodes such as aluminum foil, stainless steel, or indium tin oxide–coated glass (12, 14, 18, 88, 107). In principle, the top-down synthetic approach can also lead to single-crystalline nanowires starting with any polycrystalline thin film as long as the grains are much larger than the nanowire diameter and the film is highly textured (i.e., all the grains are oriented in the same direction). These requirements are the same as those needed in standard thin-film solar cells to reduce recombination and have been successfully implemented in a variety of relevant materials, including silicon, cadmium telluride, CIGS, and CZTS (58, 59, 62, 108). Surface strain relaxation facilitates epitaxial growth of subsequent layers onto nanowires, whereas the radial geometry increases the defect tolerance (as discussed above), which may allow for solution-processed polycrystalline layers instead of vapor phase epitaxy. The promise of bringing multijunction solar cell fabrication costs down to near traditional thin-film costs with only a moderate efficiency loss compared with world record cells is one of the most exciting possibilities for nanowire photovoltaics.

4. REMAINING CHALLENGES AND FUTURE OUTLOOK

To bring clean power to a large fraction of the world's population, solar cells must become less expensive and use fewer natural resources. Current planar technology imposes lower limits on the quantity and quality of material that must be used to realize high-efficiency solar cells. The nanowire geometry, especially when it incorporates a radial junction, relaxes these requirements, opening up the possibility to use a small amount of abundant, nontoxic, low-cost material to make solar cells with performance close to that of current planar technology. The ability to make single-crystalline nanowires on low-cost substrates such as aluminum foil and to relax strain in subsequent epitaxial layers removes two more major cost hurdles associated with high-efficiency planar solar cells. Despite the tremendous promise offered by nanowire solar cells, some daunting challenges must be addressed before the benefits can be realized commercially. These challenges include surface and interface recombination, surface roughness, mechanical and chemical stability, fine morphology and doping control, nanowire array uniformity, and synthetic scalability. Great progress has been made in most of these areas, but much more work is needed, especially that related to understanding surfaces and interfaces. Even if nanowire devices can realize efficiencies

comparable to those of planar devices at much lower costs, practical issues that have not yet been seriously explored such as rapid scaling, integration into modules, and device packaging must be addressed. The rapid improvements in efficiency within the past five years and the potential for cost reductions far below planar limits certainly warrant further research into nanowire solar cells.

DISCLOSURE STATEMENT

The authors are not aware of any affiliations, memberships, funding, or financial holdings that might be perceived as affecting the objectivity of this review.

LITERATURE CITED

1. Ginley D, Green M, Collins R. 2008. Solar energy conversion toward 1 terawatt. *MRS Bull.* 33:355–73
2. Hochbaum AI, Yang P. 2010. Semiconductor nanowires for energy conversion. *Chem. Rev.* 110(1):527–46
3. Law M, Goldberger J, Yang P. 2004. Semiconductor nanowires and nanotubes. *Annu. Rev. Mater. Res.* 34(1):83–122
4. Tian B, Kempa TJ, Lieber CM. 2009. Single nanowire photovoltaics. *Chem. Soc. Rev.* 38(1):16–24
5. Fan Z, Ruebusch DJ, Rathore AA, Kapadia R, Ergen O, et al. 2009. Challenges and prospects of nanopillar-based solar cells. *Nano Res.* 2(11):829–43
6. Yu K, Chen J. 2008. Enhancing solar cell efficiencies through 1-D nanostructures. *Nanoscale Res. Lett.* 4(1):1–10
7. Cao L, Park J, Fan P, Clemens B, Brongersma ML. 2010. Resonant germanium nanoantenna photodetectors. *Nano Lett.* 10(4):1229–33
8. Gunawan O, Sekaric L, Majumdar A, Rooks M, Appenzeller J, et al. 2008. Measurement of carrier mobility in silicon nanowires. *Nano Lett.* 8(6):1566–71
9. Ford AC, Ho JC, Chueh Y, Tseng Y, Fan Z, et al. 2009. Diameter-dependent electron mobility of InAs nanowires. *Nano Lett.* 9(1):360–65
10. Xiang J, Lu W, Hu Y, Wu Y, Yan H, Lieber CM. 2006. Ge/Si nanowire heterostructures as high-performance field-effect transistors. *Nature* 441(7092):489–93
11. Garnett E, Yang P. 2010. Light trapping in silicon nanowire solar cells. *Nano Lett.* 10(3):1082–87
12. Law M, Greene LE, Johnson JC, Saykally R, Yang P. 2005. Nanowire dye-sensitized solar cells. *Nat. Mater.* 4(6):455–59
13. Wang K, Chen JJ, Zeng ZM, Tarr J, Zhou WL, et al. 2010. Synthesis and photovoltaic effect of vertically aligned ZnO/ZnS core/shell nanowire arrays. *Appl. Phys. Lett.* 96(12):123105
14. Fan Z, Razavi H, Do J, Moriwaki A, Ergen O, et al. 2009. Three-dimensional nanopillar-array photovoltaics on low-cost and flexible substrates. *Nature Mater.* 8(8):648–53
15. Lévy-Clément C, Tena-Zaera R, Ryan MA, Katty A, Hodes G. 2005. CdSe-sensitized *p*-CuSCN/nanowire *n*-ZnO heterojunctions. *Adv. Mater.* 17(12):1512–15
16. Yuhas BD, Yang P. 2009. Nanowire-based all-oxide solar cells. *J. Am. Chem. Soc.* 131(10):3756–61
17. Varghese OK, Paulose M, Grimes CA. 2009. Long vertically aligned titania nanotubes on transparent conducting oxide for highly efficient solar cells. *Nature Nanotechnol.* 4(9):592–97
18. Dong Y, Tian B, Kempa TJ, Lieber CM. 2009. Coaxial group III-nitride nanowire photovoltaics. *Nano Lett.* 9(5):2183–87
19. Colombo C, Heiß M, Grätzel M, Fontcuberta I, Morral A. 2009. Gallium arsenide *p-i-n* radial structures for photovoltaic applications. *Appl. Phys. Lett.* 94(17):173108
20. Briseno AL, Holcombe TW, Boukai AI, Garnett EC, Shelton SW, et al. 2010. Oligo- and polythiophene/ZnO hybrid nanowire solar cells. *Nano Lett.* 10(1):334–40
21. Greene L, Law M, Yuhas B, Yang P. 2007. ZnO-TiO$_2$ core-shell nanorod/P3HT solar cells. *J. Phys. Chem. C* 111(50):18451–56

22. Takanezawa K, Tajima K, Hashimoto K. 2008. Efficiency enhancement of polymer photovoltaic devices hybridized with ZnO nanorod arrays by the introduction of a vanadium oxide buffer layer. *Appl. Phys. Lett.* 93(6):063308

23. Wei W, Bao X, Soci C, Ding Y, Wang Z, Wang D. 2009. Direct heteroepitaxy of vertical InAs nanowires on Si substrates for broad band photovoltaics and photodetection. *Nano Lett.* 9(8):2926–34

24. Williams SS, Hampton MJ, Gowrishankar V, Ding I, Templeton JL, et al. 2008. Nanostructured titania−polymer photovoltaic devices made using PFPE-based nanomolding techniques. *Chem. Mater.* 20(16):5229–34

25. Schmidt V, Wittemann JV, Gösele U. 2010. Growth, thermodynamics, and electrical properties of silicon nanowires. *Chem. Rev.* 110(1):361–88

26. Fan HJ, Werner P, Zacharias M. 2006. Semiconductor nanowires: from self-organization to patterned growth. *Small* 2(6):700–17

27. Wacaser BA, Dick KA, Johansson J, Borgström MT, Deppert K, Samuelson L. 2009. Preferential inter-face nucleation: an expansion of the VLS growth mechanism for nanowires. *Adv. Mater.* 21(2):153–65

28. Hochbaum AI, Fan R, He R, Yang P. 2005. Controlled growth of Si nanowire arrays for device integra-tion. *Nano Lett.* 5(3):457–60

29. Perea DE, Hemesath ER, Schwalbach EJ, Lensch-Falk JL, Voorhees PW, Lauhon LJ. 2009. Direct measurement of dopant distribution in an individual vapour-liquid-solid nanowire. *Nat. Nanotechnol.* 4(5):315–19

30. Garnett EC, Tseng Y, Khanal DR, Wu J, Bokor J, Yang P. 2009. Dopant profiling and surface analysis of silicon nanowires using capacitance-voltage measurements. *Nat. Nanotechnol.* 4(5):311–14

31. Whang S, Lee S, Chi D, Yang W, Cho B, et al. 2007. B-doping of vapour–liquid–solid grown Au-catalysed and Al-catalysed Si nanowires: effects of B_2H_6 gas during Si nanowire growth and B-doping by a post-synthesis in situ plasma process. *Nanotechnology* 18(27):275302

32. Pan L, Lew K, Redwing J, Dickey E. 2005. Effect of diborane on the microstructure of boron-doped silicon nanowires. *J. Cryst. Growth* 277(1–4):428–36

33. Dick Ka, Deppert K, Karlsson LS, Wallenberg LR, Samuelson L, Seifert W. 2005. A new understanding of Au-assisted growth of III–V semiconductor nanowires. *Adv. Funct. Mater.* 15(10):1603–10

34. Persson AI, Larsson MW, Stenström S, Ohlsson BJ, Samuelson L, Wallenberg LR. 2004. Solid-phase diffusion mechanism for GaAs nanowire growth. *Nature Mater.* 3(10):677–81

35. Bierman MJ, Lau YK, Kvit AV, Schmitt AL, Jin S. 2008. Dislocation-driven nanowire growth and Eshelby twist. *Science* 320(5879):1060–63

36. Zhu J, Peng H, Marshall AF, Barnett DM, Nix WD, Cui Y. 2008. Formation of chiral branched nanowires by the Eshelby Twist. *Nat. Nanotechnol.* 3(8):477–81

37. Schmid H, Björk MT, Knoch J, Riel H, Riess W, et al. 2008. Patterned epitaxial vapor-liquid-solid growth of silicon nanowires on Si(111) using silane. *J. Appl. Phys.* 103(2):024304

38. Mårtensson T, Carlberg P, Borgström M, Montelius L, Seifert W, Samuelson L. 2004. Nanowire arrays defined by nanoimprint lithography. *Nano Lett.* 4(4):699–702

39. Zschech D, Kim DH, Milenin AP, Scholz R, Hillebrand R, et al. 2007. Ordered arrays of <100>-oriented silicon nanorods by CMOS-compatible block copolymer lithography. *Nano Lett.* 7(6):1516–20

40. Huang Z, Fang H, Zhu J. 2007. Fabrication of silicon nanowire arrays with controlled diameter, length, and density. *Adv. Mater.* 19(5):744–48

41. Garnett EC, Yang P. 2008. Silicon nanowire radial *p-n* junction solar cells. *J. Am. Chem. Soc.* 130(29):9224–25

42. Hsu C, Connor ST, Tang MX, Cui Y. 2008. Wafer-scale silicon nanopillars and nanocones by Langmuir-Blodgett assembly and etching. *Appl. Phys. Lett.* 93(13):133109

43. Huang Z, Zhang X, Reiche M, Liu L, Lee W, et al. 2008. Extended arrays of vertically aligned sub-10 nm diameter [100] Si nanowires by metal-assisted chemical etching. *Nano Lett.* 8(9):3046–51

44. Bogush GH, Tracy MA, Zukoski CF IV. 1988. Preparation of monodisperse silica particles: control of size and mass fraction. *J. Non-Cryst. Solids* 104:95–106

45. Jeong S, Hu L, Lee HR, Garnett E, Choi JW, Cui Y. 2010. Fast and scalable printing of large area monolayer nanoparticles for nanotexturing applications. *Nano Lett.* 10:2989–94

46. Ho JC, Yerushalmi R, Jacobson ZA, Fan Z, Alley RL, Javey A. 2008. Controlled nanoscale doping of semiconductors via molecular monolayers. *Nature Mater.* 7(1):62–67

47. Tian B, Zheng X, Kempa TJ, Fang Y, Yu N, et al. 2007. Coaxial silicon nanowires as solar cells and nanoelectronic power sources. *Nature* 449(7164):885–89

48. Peng K, Xu Y, Wu Y, Yan Y, Lee S, Zhu J. 2005. Aligned single-crystalline Si nanowire arrays for photovoltaic applications. *Small* 1(11):1062–67

49. Sivakov V, Andrä G, Gawlik A, Berger A, Plentz J, et al. 2009. Silicon nanowire-based solar cells on glass: synthesis, optical properties, and cell parameters. *Nano Lett.* 9(4):1549–54

50. Fang H, Li X, Song S, Xu Y, Zhu J. 2008. Fabrication of slantingly-aligned silicon nanowire arrays for solar cell applications. *Nanotechnology* 19(25):255703

51. Green MA. 1982. *Solar Cells: Operating Principles, Technology and System Applications*. Kensington, NSW, Aust.: Univ. New South Wales. 274 pp.

52. Sailor M, Ginsburg E, Gorman C, Kumar A, Grubbs RH, Lewis NS. 1990. Thin films of *n*-Si/poly-$(CH_3)_3$Si-cyclooctatetraene: conducting-polymer solar cells and layered structures. *Science* 249(4973):1146–49

53. Shiu S, Chao J, Hung S, Yeh C, Lin C. 2010. Morphology dependence of silicon nanowire/poly(3,4-ethylenedioxythiophene):poly(styrenesulfonate) heterojunction solar cells. *Chem. Mater.* 22(10):3108–13

54. Peng K, Wang X, Lee S. 2008. Silicon nanowire array photoelectrochemical solar cells. *Appl. Phys. Lett.* 92(16):163103

55. Yuan G, Zhao H, Liu X, Hasanali ZS, Zou Y, et al. 2009. Synthesis and photoelectrochemical study of vertically aligned silicon nanowire arrays. *Angew. Chem. Int. Ed.* 48(51):9680–84

56. Goodey AP, Eichfeld SM, Lew K, Redwing JM, Mallouk TE. 2007. Silicon nanowire array photoelectrochemical cells. *J. Am. Chem. Soc.* 129(41):12344–45

57. Peng K, Wang X, Wu X, Lee S. 2009. Platinum nanoparticle decorated silicon nanowires for efficient solar energy conversion. *Nano Lett.* 9(11):3704–9

58. Wu X. 2004. High-efficiency polycrystalline CdTe thin-film solar cells. *Solar Energy* 77(6):803–14

59. Ramanathan K, Contreras MA, Perkins CL, Asher S, Hasoon FS, et al. 2003. Properties of 19.2% efficiency $ZnO/CdS/CuInGaSe_2$ thin-film solar cells. *Prog. Photovolt. Res. Appl.* 11(4):225–30

60. Todorov TK, Reuter KB, Mitzi DB. 2010. High-efficiency solar cell with earth-abundant liquid-processed absorber. *Adv. Mater.* 22(20):E156–59

61. Hains AW, Liang Z, Woodhouse MA, Gregg BA. 2010. Molecular semiconductors in organic photovoltaic cells. *Chem. Rev.* 110(11):6689–735

62. Hibberd CJ, Chassaing E, Liu W, Mitzi DB, Lincot D, Tiwari AN. 2009. Non-vacuum methods for formation of Cu(In, Ga)(Se, S)$_2$ thin film photovoltaic absorbers. *Prog. Photovolt. Res. Appl.* 18(6):434–52

63. Law M, Greene LE, Radenovic A, Kuykendall T, Liphardt J, Yang P. 2006. $ZnO-Al_2O_3$ and $ZnO-TiO_2$ core-shell nanowire dye-sensitized solar cells. *J. Phys. Chem. B* 110(45):22652–63

64. Musselman KP, Wisnet A, Iza DC, Hesse HC, Scheu C, et al. 2010. Strong efficiency improvements in ultra-low-cost inorganic nanowire solar cells. *Adv. Mater.* 22(35):E254–58

65. Leschkies KS, Divakar R, Basu J, Enache-Pommer E, Boercker JE, et al. 2007. Photosensitization of ZnO nanowires with CdSe quantum dots for photovoltaic devices. *Nano Lett.* 7(6):1793–98

66. Leschkies KS, Jacobs AG, Norris DJ, Aydil ES. 2009. Nanowire-quantum-dot solar cells and the influence of nanowire length on the charge collection efficiency. *Appl. Phys. Lett.* 95(19):193103

67. Khanal DR, Wu J. 2007. Gate coupling and charge distribution in nanowire field effect transistors. *Nano Lett.* 7(9):2778–83

68. Tu R, Zhang L, Nishi Y, Dai H. 2007. Measuring the capacitance of individual semiconductor nanowires for carrier mobility assessment. *Nano Lett.* 7(6):1561–65

69. Schmidt V, Senz S, Gösele U. 2006. Influence of the Si/SiO_2 interface on the charge carrier density of Si nanowires. *Appl. Phys. A* 86(2):187–91

70. Koren E, Berkovitch N, Rosenwaks Y. 2010. Measurement of active dopant distribution and diffusion in individual silicon nanowires. *Nano Lett.* 10(4):1163–67

71. Allen JE, Hemesath ER, Perea DE, Lensch-Falk JL, Li ZY, et al. 2008. High-resolution detection of Au catalyst atoms in Si nanowires. *Nat. Nanotechnol.* 3(3):168–73

72. Perea DE, Allen JE, May SJ, Wessels BW, Seidman DN, Lauhon LJ. 2006. Three-dimensional nanoscale composition mapping of semiconductor nanowires. *Nano Lett.* 6(2):181–85

73. Oh SH, van Benthem K, Molina SI, Borisevich AY, Luo W, et al. 2008. Point defect configurations of supersaturated Au atoms inside Si nanowires. *Nano Lett.* 8(4):1016–19

74. Guichard AR, Barsic DN, Sharma S, Kamins TI, Brongersma ML. 2006. Tunable light emission from quantum-confined excitons in $TiSi_2$-catalyzed silicon nanowires. *Nano Lett.* 6(9):2140–44

75. Kelzenberg MD, Turner-Evans DB, Kayes BM, Filler MA, Putnam MC, et al. 2008. Photovoltaic measurements in single-nanowire silicon solar cells. *Nano Lett.* 8(2):710–14

76. Michalak DJ, Lewis NS. 2002. Use of near-surface channel conductance and differential capacitance versus potential measurements to correlate inversion layer formation with low effective surface recombination velocities at *n*-Si/liquid contacts. *Appl. Phys. Lett.* 80(23):4458

77. Haick H, Hurley PT, Hochbaum AI, Yang P, Lewis NS. 2006. Electrical characteristics and chemical stability of non-oxidized, methyl-terminated silicon nanowires. *J. Am. Chem. Soc.* 128(28):8990–91

78. Green MA. 1995. *Silicon Solar Cells: Advanced Principles & Practice*. Sydney, NSW, Aust.: Univ. New South Wales. 366 pp.

79. Zhang S, Hemesath ER, Perea DE, Wijaya E, Lensch-Falk JL, Lauhon LJ. 2009. Relative influence of surface states and bulk impurities on the electrical properties of Ge nanowires. *Nano Lett.* 9(9):3268–74

80. Demichel O, Calvo V, Besson A, Noé P, Salem B, et al. 2010. Surface recombination velocity measurements of efficiently passivated gold-catalyzed silicon nanowires by a new optical method. *Nano Lett.* 10(7):2323–29

81. Kayes BM, Atwater HA, Lewis NS. 2005. Comparison of the device physics principles of planar and radial *p-n* junction nanorod solar cells. *J. Appl. Phys.* 97(11):114302

82. Hecht E. 2002. *Optics*. San Francisco: Pearson. 698 pp.

83. Zhao J, Green M. 1991. Optimized antireflection coatings for high-efficiency silicon solar cells. *IEEE Trans. Electron Devices* 38(8):1925–34

84. Zhu J, Yu Z, Burkhard GF, Hsu C, Connor ST, et al. 2009. Optical absorption enhancement in amorphous silicon nanowire and nanocone arrays. *Nano Lett.* 9(1):279–82

85. Muskens OL, Rivas JG, Algra RE, Bakkers EP, Lagendijk A. 2008. Design of light scattering in nanowire materials for photovoltaic applications. *Nano Lett.* 8(9):2638–42

86. Tsakalakos L, Balch J, Fronheiser J, Korevaar BA, Sulima O, Rand J. 2007. Silicon nanowire solar cells. *Appl. Phys. Lett.* 91(23):233117

87. Tang YB, Chen ZH, Song HS, Lee CS, Cong HT, et al. 2008. Vertically aligned *p*-type single-crystalline GaN nanorod arrays on *n*-type Si for heterojunction photovoltaic cells. *Nano Lett.* 8(12):4191–95

88. Fan Z, Kapadia R, Leu PW, Zhang X, Chueh Y, et al. 2010. Ordered arrays of dual-diameter nanopillars for maximized optical absorption. *Nano Lett.* 10(10):3823–27

89. Yablonovitch E, Cody G. 1982. Intensity enhancement in textured optical sheets for solar cells. *IEEE Trans. Electron Devices* ED-29(2):300–5

90. Muskens OL, Diedenhofen SL, Kaas BC, Algra RE, Bakkers EP, et al. 2009. Large photonic strength of highly tunable resonant nanowire materials. *Nano Lett.* 9(3):930–34

91. Cao L, White JS, Park J, Schuller JA, Clemens BM, Brongersma ML. 2009. Engineering light absorption in semiconductor nanowire devices. *Nature Mater.* 8(8):643–47

92. Cao L, Fan P, Vasudev AP, White JS, Yu Z, et al. 2010. Semiconductor nanowire optical antenna solar absorbers. *Nano Lett.* 10(2):439–45

93. Cao L, Fan P, Barnard ES, Brown AM, Brongersma ML. 2010. Tuning the color of silicon nanostructures. *Nano Lett.* 10(7):2649–54

94. Zhu J, Hsu C, Yu Z, Fan S, Cui Y. 2010. Nanodome solar cells with efficient light management and self-cleaning. *Nano Lett.* 10(6):1979–84

95. Green Ma, Emery K, Hishikawa Y, Warta W. 2010. Solar cell efficiency tables (version 36). *Prog. Photovolt. Res. Appl.* 18:346–52

96. Kelzenberg MD, Boettcher SW, Petykiewicz JA, Turner-Evans DB, Putnam MC, et al. 2010. Enhanced absorption and carrier collection in Si wire arrays for photovoltaic applications. *Nat. Mater.* 9(3):239–44

97. Peters CH, Guichard AR, Hryciw AC, Brongersma ML, McGehee MD. 2009. Energy transfer in nanowire solar cells with photon-harvesting shells. *J. Appl. Phys.* 105(12):124509

98. Lu S, Lingley Z, Asano T, Harris D, Barwicz T, et al. 2009. Photocurrent induced by nonradiative energy transfer from nanocrystal quantum dots to adjacent silicon nanowire conducting channels: toward a new solar cell paradigm. *Nano Lett.* 9(12):4548–52

99. Kuykendall T, Ulrich P, Aloni S, Yang P. 2007. Complete composition tunability of InGaN nanowires using a combinatorial approach. *Nat. Mater.* 6(12):951–56

100. Wu Z, Neaton JB, Grossman JC. 2008. Quantum confinement and electronic properties of tapered silicon nanowires. *Phys. Rev. Lett.* 100:246804

101. Beard MC, Midgett AG, Hanna MC, Luther JM, Hughes BK, Nozik AJ. 2010. Comparing multiple exciton generation in quantum dots to impact ionization in bulk semiconductors: implications for enhancement of solar energy conversion. *Nano Lett.* 10:3019–27

102. Nozik AJ. 2010. Nanoscience and nanostructures for photovoltaics and solar fuels. *Nano Lett.* 10(8):2735–41

103. Wu Z, Neaton JB, Grossman JC. 2009. Charge separation via strain in silicon nanowires. *Nano Lett.* 9(6):2418–22

104. Tiedje T, Yablonovitch E, Cody G, Brooks B. 1984. Limiting efficiency of silicon solar cells. *IEEE Trans. Electron Devices* 31(5):711–16

105. Takanezawa K, Hirota K, Wei Q, Tajima K, Hashimoto K. 2007. Efficient charge collection with ZnO nanorod array in hybrid photovoltaic devices. *J. Phys. Chem. C* 111(19):7218–23

106. Kempa TJ, Tian B, Kim DR, Hu J, Zheng X, Lieber CM. 2008. Single and tandem axial *p-i-n* nanowire photovoltaic devices. *Nano Lett.* 8(10):3456–60

107. Chan CK, Peng H, Liu G, McIlwrath K, Zhang XF, et al. 2008. High-performance lithium battery anodes using silicon nanowires. *Nat. Nanotechnol.* 3(1):31–35

108. Green M, Basore P, Chang N, Clugston D, Egan R, et al. 2004. Crystalline silicon on glass (CSG) thin-film solar cell modules. *Solar Energy* 77(6):857–63

Contents

Index

Errata

An online log of corrections to *Annual Review of Materials Research* articles may be found at http://matsci.annualreviews.org/errata.shtml